

DETERMINATION OF CORRECTIONS TO
FLOW DIRECTION MEASUREMENTS OBTAINED WITH A
WING-TIP MOUNTED SENSOR

By

Thomas Martin Moul

B.S. May 1977, University of Virginia

(NASA-CR-174412) DETERMINATION OF
CORRECTIONS TO FLOW DIRECTION MEASUREMENTS
OBTAINED WITH A WING-TIP MOUNTED SENSOR
M.S. Thesis (George Washington Univ.) 91 p
HC A05/MP A01

N85-18962

Unclas
18137

CSCI 01A G3/C2

A Thesis submitted to
the Faculty of

The Graduate School of Engineering and Applied Science
of the George Washington University in partial satisfaction
of the requirements for the degree of Master of Science

August 1983

ABSTRACT

An investigation into the nature of corrections for flow direction measurements obtained with a wing-tip mounted sensor has been conducted. Corrections for the angles of attack and sideslip, measured by sensors mounted in front of each wing tip of a general aviation airplane, have been determined. These flow corrections have been obtained from both wind-tunnel and flight tests over a large angle-of-attack range. Both the angle-of attack and angle-of-sideslip flow corrections were found to be substantial. The corrections were a function of the angle of attack and angle of sideslip. The effects of wing configuration changes, small changes in Reynolds number, and spinning rotation on the angle-of-attack flow correction were found to be small. The angle-of-attack flow correction determined from the static wind-tunnel tests agreed reasonably well with the correction determined from flight tests.

ACKNOWLEDGEMENTS

The author wishes to thank the National Aeronautics and Space Administration for providing the opportunity to perform this research, prepare this thesis, and complete all the other requirements for this degree. The author is grateful to Professor John P. Campbell who acted as my academic and thesis advisor. His guidance and encouragement have been instrumental in the successful completion of my degree program. I would also like to thank Mr. William P. Gilbert for his timely review of the thesis and his helpful comments and Ms Nadine E. McHatton for her speedy preparation of this document. Special thanks also go to Mr. Eric C. Stewart for his advice and encouragement, Mr. Kenneth E. Glover for supplying me with the spin flight-test data used in this thesis, and Mr. Randy S. Hultberg for supplying me with the rotary-balance data used in this thesis. Finally, I would like to thank Dr. Vladislav Klein and Dr. Michael K. Myers for reviewing my thesis and serving on my thesis defense committee.

TABLE OF CONTENTS

	Page
TITLE	i
ABSTRACT	ii
ACKNOWLEDGEMENTS	iii
TABLE OF CONTENTS	iv
LIST OF TABLES	v
LIST OF FIGURES	vi
LIST OF SYMBOLS	ix
Chapter	
I INTRODUCTION	1
II TEST CONFIGURATIONS	4
III DATA ACQUISITION EQUIPMENT	6
IV TEST TECHNIQUES AND TEST CONDITIONS	10
V ANALYSIS TECHNIQUES	13
VI RESULTS AND DISCUSSION	22
VII SUMMARY OF RESULTS	31
APPENDIX	32
REFERENCES	39
TABLES	41
FIGURES	43

LIST OF TABLES

	Page
1. Characteristics of research airplane	41
2. Measurement list for research airplane	42

LIST OF FIGURES

	Page
1. Scope of the NASA Langley stall/spin research program	43
2. Spin research airplane in flight	44
3. Three-view drawing of spin research airplane. Dimensions in meters (feet)	45
4. Wing leading-edge droop modification	46
5. Dimensions of the 1/6-scale model in centimeters (inches)	47
6. Definition of body axis system. Arrows indicate positive direction of quantities	48
7. Flow direction sensor used in the wind-tunnel tests	49
a. Photograph of the flow direction sensor.	
b. Dimensions (in cm) of the flow direction sensor.	
8. Flow direction and velocity sensor used in the flight tests	50
9. Model mounted in the 12-foot low-speed wind tunnel	51
10. Model with the outboard leading-edge droop modification applied to the wings	52
11. Definition of the angles measured to determine the angle-of-attack flow correction	53
12. Model mounted on the rotary-balance apparatus in the spin tunnel .	54
13. Definition of the angle-of-attack and angle-of-sideslip flow correction	55
a. Definition of the angle-of-attack flow correction.	
b. Definition of the angle-of-sideslip flow correction.	
14. Longitudinal force and moment data for the model	56
15. Resultant-force coefficient data for the model	57
16. The effect of leading-edge modifications on the lift coefficient of the model	58
17. The effect of the Reynolds number on the lift coefficient of the model	59

18.	The true versus the measured angle of attack from the static wind-tunnel tests	60
19.	The angle-of-attack flow correction determined from the static wind-tunnel tests	61
20.	The effect of the outboard droop leading-edge modification on the angle-of-attack flow correction determined from the static wind-tunnel tests	62
21.	The effect of the full-span droop leading-edge modification on the angle-of-attack flow correction determined from the static wind-tunnel tests	63
22.	The effect of aileron deflections on the angle-of-attack flow correction determined from the static wind-tunnel tests	64
23.	The effect of the outboard droop modification and an aileron deflection on the angle-of-attack flow correction determined from the static wind-tunnel tests	65
24.	The effect of the Reynolds number on the angle-of-attack flow correction determined from the static wind-tunnel tests	66
25.	The effect of the sensor location on the angle-of-attack flow correction determined from the static wind-tunnel tests	67
26.	The effect of the sideslip angle on the angle-of-attack flow correction determined from the static wind-tunnel tests	68
27.	The angle-of-sideslip flow correction determined from the static wind-tunnel tests	69
28.	The effect of the full-span droop leading-edge modification on the angle-of-sideslip flow correction determined from the static wind-tunnel tests	70
29.	The effect of the sideslip angle on the angle-of-sideslip flow correction determined from the static wind-tunnel tests	71
30.	The effect of the angle of attack on the angle-of-sideslip flow correction determined from the static wind-tunnel tests	72
31.	The effect of rotation on the angle-of-attack flow correction determined in the spin tunnel. Determined from different rates of rotation at $\alpha_{t_{cg}} = 40^\circ$	73
32.	The effect of rotation on the angle-of-attack flow correction determined in the spin tunnel. Determined from different angle-of-attack settings at $\Omega b/2V = -.3$	74

33.	Comparison of the angle-of-attack flow correction determined from static wind-tunnel tests and from level flight tests	75
34.	Comparison of the angle-of-attack flow correction determined from static wind-tunnel tests and from two approximate methods used during steady spins	76
35.	Comparison of the angle-of-attack flow correction determined from static wind-tunnel tests and from a steady spin analysis technique	77
36.	Instantaneous arrangement of ground axis system	78
37.	Relationship between resultant acceleration and resultant rotation vectors	79

LIST OF SYMBOLS

\bar{A}	resultant acceleration, g units
\bar{A}_C	centrifugal acceleration, m/sec^2 (ft./sec ²)
\bar{A}_X, \bar{A}_Z	linear accelerations along the X_g, Z_g ground axes, g units
a_w	acceleration along velocity vector, g units
a_x, a_y, a_z	linear accelerations along the X_b, Y_b, Z_b body axes, g units
b	wing span, m (ft)
C	constant, $\frac{1}{\cos \beta} (1 + a_y \sin \beta)$
C_D	drag coefficient, Drag/ $q_\infty S$
C_L	lift coefficient, Lift/ $q_\infty S$
C_R	resultant-force coefficient, $\sqrt{C_D^2 + C_L^2}$
C_m	pitching-moment coefficient, positive nose up, Pitching moment/ $q_\infty S \bar{c}$
\bar{c}	wing mean aerodynamic chord, m (ft)
F_w	force along velocity vector, N (lb)
g	acceleration due to gravity, m/sec^2 (ft./sec ²)
h	altitude, m (ft)
\dot{h}	altitude rate, m/sec (ft./sec)
$\hat{I}, \hat{J}, \hat{K}$	unit vectors along the X_g, Y_g, Z_g ground axes
$\hat{i}, \hat{j}, \hat{k}$	unit vectors along the X_b, Y_b, Z_b body axes
i, j, k	direction components of \bar{X}_g' in the body axes
L_{bw}	transformation matrix from wind axes to body axes
l_J, m_J, n_J	direction cosines in the body axis system of the J ground axis
l'_j, m'_j, n'_j	direction cosines in the ground axis system of the j body axis
m	mass, kg (slugs)
p, q, r	angular velocity about the X_b, Y_b, Z_b body axes, rad/sec (deg/sec)
q_∞	free-stream dynamic pressure, Pa (lb/ft ²)

R_n	Reynolds number, $\frac{V\bar{C}}{\nu}$
R_s	radius of the spin, m (ft)
S	wing area, m^2 (ft ²)
U, V, W	linear velocities along the X_g, Y_g, Z_g ground axes, m/sec (ft/sec)
u, v, w	linear velocities along the X_b, Y_b, Z_b body axes, m/sec (ft/sec)
V	total velocity, m/sec (ft/sec)
\bar{V}	total velocity vector, m/sec (ft/sec)
$V_{\lambda,c}$	local flow velocity with the boom and flow direction sensor in the calibration apparatus, m/sec (ft/sec)
$V_{\lambda,m}$	local flow velocity with the boom and flow direction sensor mounted on the model, m/sec (ft/sec)
W	weight, N(lb)
X_b, Y_b, Z_b	body axes
X_g, Y_g, Z_g	ground axes
\bar{X}_g'	vector along the X_g ground axis
x, y, z	distance along X_b, Y_b, Z_b body axes, from cg to flow direction sensors, m (ft)
α	angle of attack, rad (deg)
α_m	measured angle of attack, rad (deg)
α_t	true angle of attack, rad (deg)
β	angle of sideslip, rad (deg)
β_m	measured angle of sideslip, rad (deg)
β_t	true angle of sideslip, rad (deg)
γ	flight path angle, rad (deg)
δ	helix angle of flight path measured from the vertical, rad (deg)
δ_a	aileron deflection, rad (deg)

δ_e	elevator deflection, rad (deg)
δ_r	rudder deflection, rad (deg)
ϵ_α	angle-of-attack flow correction, rad (deg)
ϵ_β	angle-of-sideslip flow correction, rad (deg)
θ	airplane pitch attitude, rad (deg)
θ_s	wind tunnel mounting strut angle, rad (deg)
μ	angle between flight path and X_b body axis, rad (deg)
ν	kinematic viscosity, m^2/sec (ft^2/sec)
σ	angle between resultant acceleration and resultant rotation vectors, rad (deg)
Ω	angular velocity about spin axis, rad/sec (deg/sec)
$\vec{\Omega}$	angular velocity vector, rad/sec (deg/sec)
$\frac{\Omega_b}{2V}$	spin coefficient, positive for clockwise spins

Subscripts

b	body axis system
cg	at the center-of-gravity location
g	ground axis system
l	left
m	measured
r	right
s	at the sensor location
t	true
w	wind axis system

Abbreviations

cg	center of gravity
psf	lb/ft ²
psi	lb/in ²

CHAPTER 1

INTRODUCTION

In quantitative flight-test investigations it is often desirable to reduce the flight data to a form that can be compared directly with wind-tunnel data or theoretical predictions. An essential flight quantity for this comparison is the true angle of attack of the airplane. Typically, the angle of attack during flight tests is measured with a self-aligning vane or flow direction sensor (ref. 1). The sensor is often mounted on booms ahead of the wing near each wing tip and measures the local flow direction. To determine the true angle of attack of the airplane, corrections must be applied to this measured local flow direction (called the measured angle of attack herein) to account for the change in the flow direction at the sensor location due to the presence of the airplane.

For airplanes in the normal, unstalled flight regime, this flow correction may be easily determined both experimentally from flight tests and theoretically (ref. 2). Experimentally, when an airplane is in steady, straight and level flight the true angle of attack is given either by the pitch attitude measurement or by the inverse sine of the longitudinal acceleration measurement (refs. 3 and 4). Theoretically, the flow correction in front of the wing may be determined using lifting line theory (refs. 5 and 6).

However, at angles of attack above the stall these methods are no longer usable. The flight test technique cannot be used because the airplane can no longer achieve steady level flight at angles of attack above the stall. Also, the lifting line theory is no longer valid due to the separated flow over the wing. In fact, the nature of the flow correction at these large angles of attack is not well known.

One field of study where the knowledge of this correction at large angles of attack is needed is in spin-flight testing. The NASA Langley Research Center is conducting a comprehensive stall/spin investigation of general aviation airplanes to help improve their safety. The program includes the use of full-scale and radio-controlled model flight tests, static wind-tunnel tests of full-scale airplanes and models, spin-tunnel tests, rotary-balance tests, and computer simulation studies (fig. 1). At the large angles of attack encountered during the stall/spin flight tests, the flow correction is substantial and, therefore, it must be applied to the flight data to enable correlation with data from other phases of the stall/spin program (ref. 7). Also, any theoretical approach to the stall/spin problem would require the true angle of attack to be known. Thus, an understanding of the flow correction at large angles of attack is important in the study of the general aviation stall/spin problem.

Preliminary investigations into the nature of the flow correction at large angles of attack have shown that the correction can be substantial (refs. 8 and 9). These reports looked only briefly at the flow correction encountered on one of the research airplanes involved in the Langley stall/spin program. It was deemed necessary to undertake a more thorough study into the basic nature of the flow correction. It was also desirable to expand the data base for the stall/spin program by obtaining flow correction data for another research airplane utilized in the program.

This thesis presents the results of a study to determine the flow correction to be applied to the measurement of the angles of attack and sideslip over a large angle-of-attack range. This work includes the determination of the flow correction from both wind-tunnel and flight tests of

one of the general aviation research airplanes utilized in the Langley stall/spin program.

A 1/6-scale model of the general aviation research airplane was tested by the author in a low-speed wind tunnel at the Langley Research Center. The model was tested over a large angle-of-attack range and the effects on the flow correction due to changes in flow parameters and configuration changes were determined. The same model was also tested on the rotary-balance apparatus located in the Langley Spin Tunnel. The author analyzed this data to evaluate the effect of rotation on the flow correction.

The general aviation research airplane was flown in both level flight and spinning flight as part of the Langley stall/spin program. The author used the data from the level flight tests to determine a low angle-of-attack flow correction. Data from many different spin flight tests were analyzed by the author. The author applied two approximate methods and a more complete analytical method to determine the flow correction during these spins. The angle-of-attack flow correction determined by using these methods is presented herein. However, the methods did not satisfactorily determine the angle-of-sideslip flow correction; therefore, no data are presented for this parameter.

CHAPTER 2

TEST CONFIGURATIONS

Flight Test Airplane

A single-engine, low wing, general aviation spin research airplane (fig. 2) was used in the flight tests reported herein. A three-view drawing of the airplane is shown in figure 3. Some of the pertinent physical characteristics of the airplane are given in Table 1.

The airplane was equipped with two spin recovery systems. The primary spin recovery system utilized hydrogen peroxide rockets mounted on each wing tip (ref. 10). The research pilot could select which rocket to fire to produce an unbalanced yawing moment to oppose the spin aerodynamic moments. The rockets could also be fired in a direction to enhance the aerodynamic moments in order to transition the airplane to a higher angle-of-attack spin mode. The airplane was also equipped with a spin recovery parachute.

Many modifications to the wing and body were flight tested to evaluate their effect on the spin characteristics of the airplane. One of the wing modifications was found to improve the stall/spin characteristics of the airplane (ref. 11). This modification consisted of a glove over the forward part of the airfoil which provided a 3-percent chord extension and a droop which increased the leading-edge camber and radius (fig. 4). This leading-edge modification could be added to the full span of the airplane wing, but was segmented so that different spanwise lengths could also be tested.

Wind-Tunnel Model

The 1/6-scale model of the spin research airplane was tested in the 12-foot low-speed wind tunnel and in the spin tunnel at the NASA Langley Research Center. The model was constructed of fiberglass, wood, and aluminum. The model did not have landing gear and had the propeller removed for the tests. The rear fuselage section, including the horizontal and vertical tails, was removed to facilitate mounting the model in the 12-foot wind tunnel. A drawing of the model as tested in the 12-foot tunnel is shown in figure 5. In the spin tunnel, the model was tested with both the horizontal and vertical tails on.

The model had movable ailerons allowing deflections of up to $\pm 25^\circ$. A scaled version of the leading-edge droop modification tested in flight could be applied to the forward portion of the model airfoil. This droop modification was also segmented so different spanwise lengths could be tested.

CHAPTER 3

DATA ACQUISITION EQUIPMENT

Equipment Used in Wind-Tunnel Tests

Static tests.- Aerodynamic forces and moments acting on the model were measured with an internally mounted, six-component strain-gauge balance. The balance measured the normal, axial, and side forces and the rolling, yawing, and pitching moments acting about the model body axes (fig. 6). The interactions that existed between the six-components were determined by balance calibration tests and were accounted for after the balance voltages were converted to forces and moments. The moment data were non-dimensionalized and presented as body axis rolling, yawing, and pitching moment coefficients for a center-of-gravity position of $.21\bar{c}$. The force data were non-dimensionalized and transferred to the stability axis system and presented as lift, drag, and side-force coefficients.

The model was equipped with two flow direction sensors (fig. 7) similar to those described in reference 1. These sensors were part of a prototype data system developed at the Langley Research Center for use in quantitative flight testing of radio-controlled models. The flow direction sensors were equipped with two potentiometers--one each for the measurement of the angles of attack and sideslip. The potentiometers produced a voltage which was proportional to the sensor angular position.

The output voltages from the strain-gauge balance and the flow direction sensors were hard-wired to the control room. These low level analog output signals were converted to digital form by the NEFF 620 amplifier/multiplexor. The NEFF 620 provided the required signal

conditioning, amplification, filtering, and multiplexing. The digital output from the NEFF 620, in 16-bit binary word format, was fed into a HP-9845B mini-computer. At each test condition, the measured parameters were sampled 100 times over a period of about 21 seconds. The computer averaged these 100 measurements and converted the average to engineering units. Print-outs and plots of the data were available on the CRT display and/or the printer. The reduced data were stored on a magnetic tape.

The flow direction sensors were mounted on a 6.44 mm (.25 in.) diameter cylindrical rod which positioned them in front of each wing tip. The sensor pivot was located 17.7 cm (6.97 in.) or $.79\bar{c}$ in front of the leading edge of the wing. The pivot was located 73.5 cm (28.9 in.) outboard from the center line of the model. The sensors were instrumented to measure the local angles of attack and sideslip.

The flow direction sensors were thoroughly calibrated once they were installed on the model in the tunnel. Both the angle-of-attack and angle-of-sideslip sensors were calibrated using a specially designed calibration protractor. These calibrations were checked daily for changes in the zero values. Under these closely controlled conditions, the angle-of-attack measurements were repeatable within 1° . Because the sideslip potentiometer was smaller and less sophisticated than the angle-of-attack potentiometer, the angle-of-sideslip measurements were repeatable to within only 2° .

Rotary tests.- A six-component strain-gauge balance was used to measure the forces and moments acting on the model while subjected to rotational flow conditions. As in the static tests, the strain-gauge balance measured the forces and moments acting about the model body axes. Again, the data were adjusted to account for the balance interactions. The data

were non-dimensionalized and presented as body axis force and moment coefficients for a center-of-gravity position of $.21\bar{C}$.

The model was equipped with two flow direction sensors similar to those used in the static tests. As in the static tests, the sensors were used to measure the local angles of attack and sideslip. The data acquisition, reduction, and presentation system was composed of a 12-channel scanner/voltmeter, a HP-9845B mini-computer, and a plotter. This equipment provided on-line digital print-out and graphical plots of the data.

Equipment Used in Flight Tests

An analog data system with 20 channels of continuous FM data and 28 channels of time-shared data was installed on the airplane. The measured data were stored on a 9-track magnetic tape at a rate of 20 times per second. The measured parameters included the true airspeed and flow angles at each wing tip, linear accelerations, angular rates, Euler attitudes, control positions and forces, altitude, and altitude rate. The complete measurement list is shown in Table 2.

The airplane was equipped with a flow direction and velocity sensor (ref. 1) mounted on a boom ahead of each wing tip (fig. 8). Each sensor pivot was located 1.06 m (3.49 ft.) in front of the wing and 4.41 m (14.47 ft.) outboard from the airplane center line. The sensors measured the angles of attack and sideslip and the true airspeed of the airplane. The angle-of-attack and angle-of-sideslip sensors were calibrated before each flight. The accuracy of the angle-of-sideslip sensor was about $1/2^\circ$ while the accuracy of the angle-of-attack sensor was about 1° (ref. 3).

Linear accelerations were measured by a triad of accelerometers mounted on the floor near the airplane center-of-gravity location. Angular rates were measured by three rate gyros mounted orthogonally on a two-level instrumentation rack. The rack was located behind the front seats and also contained the attitude gyros, signal conditioning equipment, power supplies, and tape recorder.

CHAPTER 4

TEST TECHNIQUES AND TESTS CONDITIONS

Wind-Tunnel Tests

Static tests.- The 1/6-scale model of the research airplane was tested at the Langley Research Center in the 12-foot low-speed wind tunnel which has a 3.66 m (12 ft.) octagonal test section. Figure 9 shows the model mounted in the wind tunnel. Most of the tests were conducted at a free stream dynamic pressure of 4 psf which corresponded to a Reynolds number of 0.27×10^6 , based on the mean aerodynamic chord of the wing. Data were obtained over an angle-of-attack range from 0° to 85° and an angle-of-sideslip range from -20° to 20° . No corrections were made to the data for jet boundary, blockage, or wall effects. Because the force and moment data were used only to show trends, the data were not corrected for upwash (about 2° for this test).

The leading-edge droop modification discussed previously was tested in two lengths. The outboard droop extended from 57- to 95-percent $b/2$ on each wing and the full-span droop extended from the fuselage to 95-percent $b/2$ on each wing. Figure 10 shows the outboard droop leading-edge modification attached to the model. The effects of aileron deflections, sensor location, angle of sideslip, and Reynolds number on the flow correction were also investigated.

To account for flow irregularities in the tunnel, a calibration was conducted. To accomplish this, the boom and sensor were removed from the model and placed in a calibration apparatus. This apparatus positioned the boom and sensor at the same point in the tunnel as they were when mounted on the model. With the model out of the tunnel and the boom and sensor in

this calibration setup, the sensor measured the true or free-stream angles of attack and sideslip as a function of the model mounting strut angle, θ_s (fig. 11(a)). Calibration runs were made at angles of sideslip from -20° to 20° and at angles of attack from 0° to 85° .

After the calibration runs were made, the boom and the sensor were mounted on the model and the model tests were started. In this configuration the sensor gave the measured angles of attack and sideslip as a function of the mounting strut angle (fig. 11(b)).

Rotary tests.- The 1/6-scale model of the research airplane was also tested in the Langley Spin Tunnel using the rotary-balance apparatus (fig. 12 and ref. 12). The tests were conducted at an airstream velocity of 7.6 m/sec (25 ft/sec) which corresponded to a Reynolds number of $.12 \times 10^6$ based on the mean aerodynamic chord of the wing. The model was tested over an angle-of-attack range from 8° to 90° at a zero sideslip angle. At each angle of attack both static and rotary data were obtained. The rates of rotation included $\frac{\Omega b}{2V}$ values of .1, .2, .3, .4, .5, .6, .7, .8, and .9 in both clockwise and counter-clockwise directions.

A calibration to account for flow irregularities in the spin tunnel was not conducted. It was felt that a flow calibration was not as necessary in the spin tunnel as it was in the 12-foot low-speed wind tunnel. This was due to the fact that during the rotary tests, data were taken as the flow direction sensors swept around the tunnel, thus helping to average out the flow irregularities. One data point was the average of 80 measurements. That is, 8 measurements were taken during each revolution for a total of 10 revolutions. Also, the static data were the average of 4 measurements, each taken with the model rotated 90° from the previous orientation.

Flight Tests

Level flight tests.- The spin research airplane was flown in steady, straight and level flight at different airspeeds to obtain an airspeed and angle-of-attack calibration. Data were taken at airspeeds ranging from the maximum cruise speed to the minimum speed at which the airplane could maintain steady, level flight. At each airspeed the airplane was flown in opposite directions and the results of the two runs were averaged. The flight was made on a calm day at an altitude close to sea level. From these runs a low angle-of-attack flow correction was determined.

Spin flight tests.- The research airplane was flight tested as part of the Langley Research Center's general aviation stall/spin program. The spin flight tests were conducted at the NASA Wallops Flight Center. Each spin attempt was started at an altitude above 2438 m (8,000 ft.), often close to 3048 m (10,000 ft.). Spins were entered by slowly decelerating at idle power to a 1-g wings-level stall. At the stall break, prospin rudder was applied followed by ailerons against the spin once the wing had dropped 90°. On some of the spin flights the rocket system was actually fired in a pro-spin direction. This was done to increase the spin rate of the airplane in order to look for high angle-of-attack spin modes. During the spin research program the airplane was flown with different center-of-gravity locations and with a number of different leading-edge modifications. Data from many different steady spins were used to determine the true angle of attack in the spin.

CHAPTER 5

ANALYSIS TECHNIQUES

Static Wind-Tunnel Tests

To determine the flow correction, data from the desired model-in data run as well as data from the appropriate calibration run were used. The angle-of-attack flow correction, ϵ_α , was the difference between the measured and the true angles of attack at a particular strut angle (fig. 13(a)), that is

$$\epsilon_\alpha = \alpha_m - \alpha_t \quad (1)$$

For data analysis, the angle-of-attack flow correction (ϵ_α), was plotted against the measured angle of attack (α_m).

Initially, the flow correction was plotted against the measured angle of attack for both the right and left sensors separately. However, this data showed some differences between the flow correction from the right sensor and the flow correction from the left sensor. This difference could be due to an asymmetric model, an asymmetric mounting of the sensors, a difference between the sensors, or a difference in the flow field from one side of the model to the other. Asymmetries in the model or between the flow sensors were not suspected so the most likely explanation was a difference in the flow field. This explanation was backed up by an earlier, unpublished flow survey of the tunnel. The survey showed as much as 2° angularity difference between the point in the tunnel where the right sensor was located and the point where the left sensor was positioned. Part of this difference was accounted for by the model-out calibration runs. However, once the model was mounted in the tunnel the flow angularity could

possibly change from the angularity that was measured during the calibration runs. To take care of this difference the flow correction from the right sensor was averaged with the flow correction from the left sensor. This average flow correction was then plotted against the average of the measured angles of attack from the right and left sensors.

To look at the effect of the angle of sideslip on the flow correction, the flow correction from the right sensor was plotted against the measured angle of attack from the right sensor. In this case, data from the right sensor were used because the tunnel survey showed that the flow quality was better on the right side of the tunnel.

The angle-of-sideslip flow correction was determined in a manner similar to the method used in the calculation of the angle-of-attack flow correction. That is, the angle-of-sideslip flow correction, ϵ_β , was the difference between the measured and the true angles of sideslip at a particular strut angle (figure 13(b)):

$$\epsilon_\beta = \beta_m - \beta_t \quad (2)$$

The angle-of-sideslip flow correction was also averaged, but in a slightly different manner. As the angle of attack increased, the noses of the sideslip sensors had a tendency to point toward the center line of the airplane. This represented a positive sideslip increment for the left sensor and a negative sideslip increment for the right sensor. Thus, if the angle-of-sideslip flow correction from both sensors was simply averaged, the resulting correction would be close to zero. To determine the magnitude of the angle-of-sideslip flow correction, the correction from the right sensor was subtracted from the correction measured by the left sensor and the result was divided in half. That is:

$$\epsilon_{\beta} = \frac{\epsilon_{\beta_l} - \epsilon_{\beta_r}}{2} \quad (3)$$

This averaged magnitude of the sideslip flow correction was then plotted against either the average measured angle of attack or the average measured sideslip angle.

Rotary Wind-Tunnel Tests

During the rotary tests, the model was set at a given true angle of attack ($\alpha_{t_{cg}}$) and true angle of sideslip ($\beta_{t_{cg}}$) and the apparatus forced the model to rotate at a selected value of the spin coefficient ($\Omega b/2V$). While the model was rotating, the angle of attack at each wing tip was measured by the flow direction sensors. To calculate the flow correction, the angle of attack at the cg was first transferred to the sensor locations. This was done by calculating the body axis velocities at the center-of-gravity location, as follows:

$$\begin{aligned} u_{cg} &= V_{cg} \cdot \cos \alpha_{t_{cg}} \cdot \cos \beta_{t_{cg}} \\ v_{cg} &= V_{cg} \cdot \sin \beta_{t_{cg}} \\ w_{cg} &= V_{cg} \cdot \sin \alpha_{t_{cg}} \cdot \cos \beta_{t_{cg}} \end{aligned} \quad (4)$$

The body velocities at the cg were then transferred to the wing tip using the corrections for vehicle rotation.

$$\begin{aligned} u_s(i) &= u_{cg} + q \cdot z(i) - r \cdot y(i) \\ v_s(i) &= v_{cg} + r \cdot x(i) - p \cdot z(i) \\ w_s(i) &= w_{cg} + p \cdot y(i) - q \cdot x(i) \end{aligned} \quad (5)$$

where (i) = right or left

Finally, the angle of attack at each wing tip was calculated:

$$\alpha_{t_s}(i) = \tan^{-1} (w_s(i)/u_s(i)) \quad (6)$$

Therefore, this calculated angle of attack (α_{t_s}) represented the true angle of attack at one of the sensor locations. These transferred true angles of attack were subtracted from the angles of attack measured by the sensors to obtain the flow correction at each wing tip.

In the presentation of the data from the rotary-balance apparatus, only the measured angle of attack at the right wing tip sensor was used. This was done because the data from the right sensor was more consistent during the static points taken during each run.

Level Flight Tests

The research airplane was flown in steady, straight and level flight and the true angle of attack was determined. In level flight, the flight path angle (γ) was zero. So from the following equation,

$$\theta = \alpha + \gamma \quad (7)$$

it can be seen that for level flight the true angle of attack equaled the pitch angle, θ . The pitch angle could be obtained in two ways. First, it was measured directly by the attitude gyros carried onboard the airplane.

Secondly, it could be determined by using the measurement of the longitudinal accelerometer. Because the airplane was in steady flight the longitudinal accelerometer was only influenced by gravity. The longitudinal acceleration reading was determined by how much the x-body axis of the airplane was inclined to the horizon. This inclination angle was nothing more than the pitch angle and was found by taking the inverse sine of the longitudinal acceleration:

$$\theta = \alpha = \sin^{-1} (a_x) \quad (8)$$

In this thesis the true angle of attack was determined using equation

8. Once the true angle of attack was known, it was subtracted from the measured angle of attack to determine the flow correction. Finally, the flow correction was plotted against the measured angle of attack to determine the flow-correction characteristics at low angles of attack.

Steady Spin Approximations

Method 1.- After the research airplane had been in a spin for six or more turns, most of the measured quantities became reasonably constant with time. By the time the spin became steady, the velocity vector had become nearly vertical. For this method, the airplane velocity vector was assumed to be oriented along the angular velocity vector. This meant that the spin axis passed through the center of gravity of the airplane. To satisfy this assumption, the airplane could not have a spin radius and thus its center of gravity could not move in a helical path.

Once this assumption was made, the airplane angular velocity vector could be transferred from the wind axis system to the body axis system as indicated in reference 13:

$$\overline{\Omega}_b = L_{bw} \overline{\Omega}_w$$

$$\begin{bmatrix} p \\ q \\ r \end{bmatrix} = \begin{bmatrix} \cos \alpha_t \cos \beta_t & -\cos \alpha_t \sin \beta_t & -\sin \alpha_t \\ \sin \beta_t & \cos \beta_t & 0 \\ \sin \alpha_t \cos \beta_t & -\sin \alpha_t \sin \beta_t & \cos \alpha_t \end{bmatrix} \begin{bmatrix} \Omega \\ 0 \\ 0 \end{bmatrix}$$

$$p = \Omega \cos \alpha_t \cos \beta_t \quad (9)$$

$$q = \Omega \sin \beta_t \quad (10)$$

$$r = \Omega \sin \alpha_t \cos \beta_t \quad (11)$$

Equations 9 and 11 were combined to give the true angle of attack at the

center of gravity of the airplane in a steady spin:

$$\alpha_{t_{cg}} = \tan^{-1}\left(\frac{r}{p}\right) \quad (12)$$

The equations for the angular rates could also be used to compute a true angle of sideslip at the center of gravity of the airplane in a steady spin. Equations 9 and 10 were combined to yield:

$$\beta_{t_{cg}} = \tan^{-1}\left(\frac{q \cdot \cos \alpha_{t_{cg}}}{p}\right) \quad (13)$$

To determine the flow correction, the measured angles of attack at the wing tips were transformed to the center-of-gravity location. This was done by first converting the flow direction and velocity sensor readings into body velocity components, yielding:

$$\begin{aligned} u_S(i) &= V_m(i) \cdot \cos \alpha_m(i) \cdot \cos \beta_m(i) \\ v_S(i) &= V_m(i) \cdot \sin \beta_m(i) \end{aligned} \quad (14)$$

$$w_S(i) = V_m(i) \cdot \sin \alpha_m(i) \cdot \cos \beta_m(i)$$

where (i) = right or left

The body velocities at the wing tip were transferred to the center-of-gravity location using the corrections for vehicle rotation as follows:

$$\begin{aligned} u_{cg}(i) &= u_S(i) + r \cdot y(i) - q \cdot z(i) \\ v_{cg}(i) &= v_S(i) + p \cdot z(i) - r \cdot x(i) \\ w_{cg}(i) &= w_S(i) + q \cdot x(i) - p \cdot y(i) \end{aligned} \quad (15)$$

The body velocities at the center-of-gravity location were first averaged and then were reconstructed into the desired information. This proceeded as follows:

$$u_{cg} = \frac{u_{cg}(L) + u_{cg}(R)}{2}$$

$$v_{cg} = \frac{v_{cg} (L) + v_{cg} (R)}{2} \quad (16)$$

$$w_{cg} = \frac{w_{cg} (L) + w_{cg} (R)}{2}$$

$$\alpha_{mCG} = \tan^{-1} (w_{cg}/u_{cg}) \quad (17)$$

$$v_{mCG} = (u_{cg}^2 + v_{cg}^2 + w_{cg}^2)^{1/2} \quad (18)$$

$$\beta_{mCG} = \sin^{-1} (v_{cg}/v_{mCG}) \quad (19)$$

Finally, the flow correction was calculated by subtracting the approximated true angle of attack at the cg (eqn. 12) from the measured angle of attack at the cg (eqn. 17).

Method 2.- Another approximation utilized the fact that once the airplane was in a steady spin it was not accelerating; therefore the total force acting on it was zero. So the sum of the forces acting on the airplane in the vertical direction had to be zero. This meant that the aerodynamic force in the vertical direction was equal and opposite to the gravity force acting on the body. The linear accelerometers measured the aerodynamic forces acting on the airplane during the spin. These body axis accelerations were resolved, as indicated in reference 14, to yield an acceleration along the velocity vector, a_w :

$$a_w = (a_x \cos \alpha_t + a_z \sin \alpha_t) \cos \beta + a_y \sin \beta \quad (20)$$

Next it was assumed that the velocity vector was aligned with the gravity vector. This meant that the spin axis passed through the center of gravity of the airplane (i.e., that the spin radius was zero). Thus the center of gravity of the airplane moved downward along the gravity vector instead of moving around the spin axis in a helical path. So for equilibrium, the aerodynamic force along the velocity vector had to be equal and opposite to

the force of gravity acting on the airplane:

$$F_w = -W = -mg$$

$$F_w = m a_w g$$

$$a_w = -1 \tag{21}$$

$$(a_x \cos \alpha_t + a_z \sin \alpha_t) \cos \beta + a_y \sin \beta = -1$$

$$a_x \cos \alpha_t + a_z \sin \alpha_t = \frac{-1}{\cos \beta} (1 + a_y \sin \beta)$$

$$\text{let } C = \frac{1}{\cos \beta} (1 + a_y \sin \beta) \tag{22}$$

$$a_z \sin \alpha_t = -a_x \cos \alpha_t - C$$

$$a_z^2 \sin^2 \alpha_t = a_x^2 \cos^2 \alpha_t + 2 a_x C \cos \alpha_t + C^2$$

$$a_z^2 - a_z^2 \cos^2 \alpha_t = a_x^2 \cos^2 \alpha_t + 2 a_x C \cos \alpha_t + C^2$$

$$(a_x^2 + a_z^2) \cos^2 \alpha_t + 2 a_x C \cos \alpha_t + C^2 - a_z^2 = 0$$

$$\cos \alpha_t = \frac{-2a_x C \pm \sqrt{4a_x^2 C^2 - 4(a_x^2 + a_z^2)(C^2 - a_z^2)}}{2(a_x^2 + a_z^2)}$$

$$\cos \alpha_t = \frac{-a_x C \pm \sqrt{a_x^2 C^2 - a_x^2 C^2 - a_z^2 C^2 + a_x^2 a_z^2 + a_z^4}}{(a_x^2 + a_z^2)}$$

$$\cos \alpha_t = \frac{-a_x C \pm a_z \sqrt{a_x^2 + a_z^2 - C^2}}{a_x^2 + a_z^2} \quad \text{the - sign gives the desired root}$$

$$\alpha_t = \cos^{-1} \left(\frac{-a_x C - a_z \sqrt{a_x^2 + a_z^2 - C^2}}{a_x^2 + a_z^2} \right) \tag{23}$$

Before the flow correction could be determined the measured angle of attack had to be transformed to the cg using the procedure outlined in equations 14 through 19.

Steady Spin Analysis

A method to calculate the flow direction angles during a steady spin was proposed in reference 15. This method has been rederived in a more detailed manner in the Appendix. The method used the linear accelerations, body angular rates, and the vertical velocity to compute the true angles of attack and sideslip at the airplane cg. Again, to calculate the flow correction, the measured angles of attack and sideslip had to be transformed to the cg as indicated above.

CHAPTER 6

RESULTS AND DISCUSSION

Static Wind-Tunnel Tests

Force and moment data.- The force and moment characteristics of the basic model are shown in figure 14. The model exhibits lift and drag characteristics typical of general aviation airplanes. The lift curve reaches a maximum value at an angle of attack of 12° . After the stall the lift curve slope becomes negative and the lift curve reaches a local minimum at an angle of attack of 20° . The lift curve exhibits a local maximum at an angle of attack between 30° and 40° after which the lift coefficient decreases continuously up to 85° angle of attack. The stall can also be determined from the drag curve as evidenced by the large increase in slope at an angle of attack of 12° . The drag coefficient continually increases from 0° to 85° angle of attack. The pitching-moment coefficient shows the configuration is unstable up to the stall angle of attack. However, this is to be expected since the model was tested without a horizontal tail.

The resultant-force coefficient, fig. 15, is a combination of the lift and drag coefficients. It exhibits the decrease in lift after the stall as well as the large rise in the drag coefficient at the larger angles of attack.

Figure 16 compares the lift coefficient data for the basic configuration with that for the model with the outboard droop and the full-span droop leading-edge modifications. The configuration with the outboard-droop modification exhibits similar stall characteristics but increased lift in the middle of the angle-of-attack range, when compared with the basic configuration. The full-span droop leading-edge modifica-

tion increases both the maximum lift coefficient attainable and the stall angle of attack. The full-span drooped wing produces more lift than the basic wing over an angle-of-attack range from 10° to 50°. These lift coefficient trends for the model with the two different leading-edge modifications are similar to the data for the same modifications tested on a different configuration in reference 16.

The effect of small changes of the Reynolds number on the lift coefficient of the model is shown in figure 17. The data show the well known increase of lift coefficient with Reynolds number (ref. 17).

Basic angle-of-attack flow correction.- A plot of the true angle of attack versus the measured angle of attack for the basic model at zero sideslip is shown in figure 18. The flow correction is the difference between the data and the $\alpha_t = \alpha_m$ line. The data was fit with a regression analysis program which gave the following 1st order fit:

$$\alpha_t = -1.22 + .870 \alpha_m \quad (24)$$

The correlation coefficient was 0.9994 which indicates that the regression equation fit the data very well. Therefore, knowing the measured angle of attack of an airplane in flight, this regression equation may be used to determine the true angle of attack of the airplane.

The flow correction corresponding to the data from figure 18 is plotted against the measured angle of attack in figure 19. The data show a reduction in the flow correction after the stall angle of attack. This reduction is due to the loss of lift on the wing after the stall. At an angle of attack of about 20°, the flow correction starts to increase again. This increase occurs at almost the same angle of attack that the lift coefficient begins increasing again. The flow correction reaches a maximum of slightly more

than 12° at a measured angle of attack of about 95° . It appears that the flow correction is dependent on the drag as well as the lift because the general shape of the flow correction curve resembles the shape of the resultant-force coefficient shown in figure 15.

From this flow correction data it may be seen that for an airplane in a flat spin (an angle of attack near 90°), using the measured angle of attack instead of the true angle of attack results in an error of 15%.

Effect of wing configuration changes.- During the course of the stall/spin program, many wing modifications were evaluated as to the degree of spin resistance they provided. Also, the effect of the controls on the spin entry, developed spin and recovery was evaluated. The addition of modifications to the wing or the deflection of the ailerons will change the flow over the wing and therefore could possibly change the flow correction. A number of tests were run to evaluate the effect of wing modifications and aileron deflections on the flow correction.

The effect on the flow correction of adding the outboard droop to the wing is shown in figure 20. The modification increases the flow correction slightly between 15° and 35° measured angle of attack. This may be due to the fact that the wing with the outboard droop modification produces a larger lift coefficient than the unmodified wing over this angle-of-attack range. This increased lift would cause increased upwash at the sensor location, which would increase the flow correction.

Adding the full-span droop to the model effects the flow correction as shown in figure 21. Again the flow correction is increased between 15° and 35° angle of attack. This increase may also be due to the larger lift coefficient produced by the wing with the full-span droop over this angle-of-attack range.

The drooped leading-edge modifications tested all seem to change the flow correction. However, the differences were never larger than 1° and often much less. The α_t vs α_m data for the full-span droop modification were fit with the n^{th} order regression program, resulting in the following fit:

$$\alpha_t = -1.49 + .870 \alpha_m \quad (25)$$

The coefficients for the regression equation for the full-span droop data were very similar to the coefficients for the basic data (eqn. 24). Thus, for the purposes of correcting the measured angles of attack in flight, the drooped leading-edge modifications cause only a slight change in the correction equation.

The effect of aileron deflection on the flow correction is shown in figure 22. Deflecting the ailerons full down slightly increases the flow correction while a full-up deflection slightly decreases the flow correction. This change in the flow correction could be related to the fact that the deflection of the ailerons probably alters the lift on the wing.

One test was run with the ailerons deflected full up at the same time the outboard-droop modification was mounted on the wing. The flow correction for this configuration is shown in figure 23. Again, the flow correction is changed slightly which is likely related to the change of flow over the wing due to the wing modifications.

Effect of Reynolds number.- The effect of the test Reynolds number on the flow correction is shown in figure 24. The tunnel was run at dynamic pressures of 3, 4, and 5 which resulted in Reynolds numbers of $.23 \times 10^6$, $.27 \times 10^6$ and $.30 \times 10^6$, respectively. The flow correction appears to increase as the Reynolds number increases. This is most likely related to

the increase of lift coefficient with Reynolds number as shown in figure 17.

Effect of sensor location.- For one test, the flow direction sensors were moved forward until the pivot point was 23.7 cm (9.35in.) or $1.06 \bar{c}$ in front of the wing. As can be seen in figure 25 this change decreased the flow correction. This is as expected because as the sensors are moved forward, the influence of the wing on the flow at the sensors is reduced. This sensor location is the same distance (measured in wing chords) in front of the wing as the sensor used in the tests reported in reference 9. In both tests the airfoils used were 60 series airfoils and both tests exhibited a maximum flow correction of about 10° at a measured angle of attack of 90° . This indicates that the flow correction is not affected by small changes in the airfoil section.

Effect of angle of sideslip.- The effect of the angle of sideslip on the angle-of-attack flow correction was also investigated. Figure 26 shows the flow correction as a function of the measured angle of attack for the right flow direction sensor. At angles of attack larger than 50° , the flow correction is reduced for positive angles of sideslip and is increased for negative angles of sideslip. Apparently, the lift at the right wing tip is increased for negative sideslip angles and decreased for positive sideslip angles. Reference 17 shows similar trends, indicating that as the sweep angle of a wing is increased, the lift is shifted from the upstream to the downstream areas of the wing. However, this sweep effect would be expected to occur primarily at angles of attack below the stall and therefore may not exist at the larger angles of attack where the flow correction is affected by the angle of sideslip.

Basic angle-of-sideslip flow correction.- The flow correction to be applied to the angle-of-sideslip measurements, is shown in figure 27, as a function of the average measured angle of attack. This figure shows that the sideslip flow correction is also significant. The correction reaches a maximum of about 7° at the large measured angles of attack. This means that at the sensor location the local flow is skewed outboard by up to 7° at each wing tip. So if there is a need to know the angle of sideslip in a spin accurately, the angle of sideslip flow correction should be applied to the measured sideslip angles. To correct the measured sideslip angles, the average angle-of-sideslip flow correction presented in figure 27, should be added to the measured sideslip angle at the right sensor and subtracted from the measured sideslip angle at the left sensor.

Effect of full-span droop modification.- The effect on the sideslip flow correction of adding the full-span droop leading-edge modification to the model is shown in figure 28. The main difference is that the addition of the wing modification reduces the sideslip flow correction over an angle-of-attack range from 15° to 40° . The model has more lift in this angle-of-attack range with the leading-edge modification on the wing. This increases the wing loading and may tend to reduce the spanwise flow, thus reducing the sideslip flow correction in this region.

Effect of angle of sideslip.- Figure 29 shows the effect of the angle of sideslip on the sideslip flow correction as a function of the measured angle of attack. The main effect of sideslipping the model is to reduce the sideslip flow correction at large angles of attack.

Effect of angle of attack.- The variation of the sideslip flow correction with the measured angle of sideslip, for different angles of

attack, is shown in figure 30. At low angles of attack the sideslip flow correction is basically unchanged by the angle of sideslip. However, at larger angles of attack, the sideslip flow correction exhibits a strong dependence on the sideslip angle. Again, it can be seen that the sideslip flow correction increases with the angle of attack.

Rotary Wind-Tunnel Tests

The previous section presented the results of the flow correction determined by static wind-tunnel tests. This flow correction could be applied to angle-of-attack data measured onboard an airplane during a spin. Since the spin is an unsteady, rotational flight condition, however, it is possible that a statically determined flow correction would not be adequate in this situation. To determine if the static correction could be used, the effect of rotation on the flow correction was investigated.

For this investigation the rotary-balance apparatus in the Langley Spin Tunnel was used. The rotary-balance apparatus was found to have some freedom of movement in the pitch direction. This freedom of movement resulted in inaccurate data for the large rotation rates at the large angles of attack. To avoid this region of uncertainty, data for lower angles of attack and lower spin rates were used.

The first set of data used was from a run made with the model set at a true angle of attack of 40° with rates of rotation from $\frac{\Omega b}{2V}$ of $-.8$ to $.8$. By using data over the full range of rotation, the measured angle of attack at the right sensor varied from about 10° to 90° . In figure 31, this flow correction data is compared with the static flow correction obtained in the spin tunnel. Although there is considerable scatter in the data, the two sets of data agree fairly well.

The second set of data used was for a rotation rate of $\frac{\Omega_b}{2V} = -.3$ over an angle-of-attack range from 20° to 90° . This also resulted in a measured angle-of-attack range at the right sensor from 10° to 90° . The flow correction for this method is shown in figure 32 along with the spin tunnel static flow correction. Again, there is some scatter in the data but the two data sets show the same trend. From the data presented in figures 31 and 32, it appears that the presence of rotation does not greatly affect the statically determined flow correction.

Level Flight Tests

The airplane was flown in steady, straight and level flight to determine a low angle of attack flow correction. This data was not available for the basic airplane so data taken with the outboard droop modification on the wing were used. Figure 33 shows the comparison of the static wind-tunnel data to the low angle of attack flight data. It can be seen that the wind-tunnel and flight data are in general agreement in this angle-of-attack range.

Spin Flight Tests

Data from 15 steady spins were analyzed using the two approximate methods and the method described in the Appendix. Some spins with different leading-edge modifications were used in order to find different spin modes to cover a range of measured angles of attack. Data were also used from spins where the rockets were fired in a pro-spin direction to obtain spin modes at large angles of attack.

Steady spin approximations.- The two approximate techniques, used to

estimate the true angle of attack of the airplane in a spin, were used with some success. Figure 34 shows the angle-of-attack flow correction determined from the two techniques. The data shown are the results for the best 8 spins for each method. The data show a reasonable amount of scatter indicating that these methods probably should not be used if accurate results are needed. However, these methods do indicate the trends of the data. So if no wind-tunnel data are available these methods could be used to get an estimate of the angle-of-attack flow correction. Method #1 did not give satisfactory results for the sideslip angle during the spin; therefore, no angle-of-sideslip flow correction data are presented.

Steady spin analysis.- The angle-of-attack flow correction, determined using the steady spin analysis, is shown in figure 35. The data shown are the results of the analysis applied to 9 steady spins. The steady spin analysis seemed to better determine the angle-of-attack flow correction than the approximate methods. In fact, it is encouraging that the wind-tunnel data agree with the flight data as well as they do. In general the method did not give reasonable results for the angle-of-sideslip flow correction; thus no data are presented.

CHAPTER 7

SUMMARY OF RESULTS

The results of this investigation, to determine corrections for flow direction measurements, may be summarized as follows:

1. The flow corrections to be applied to both the measured angle of attack and measured angle of sideslip were found to be substantial.
2. The angle-of-attack flow correction appears to be a function of the aerodynamic forces acting on the model.
3. The effects of wing configuration changes and small Reynolds number changes on the angle-of-attack flow correction were found to be small.
4. The angle of sideslip had a significant effect on both the angle-of-attack and angle-of-sideslip flow corrections at large angles of attack.
5. The presence of spinning rotation did not appreciably alter the angle-of-attack flow correction.
6. The angle-of-attack flow correction determined from the static wind-tunnel tests was in agreement with the correction determined in level flight.
7. The approximate analytical methods used to determine the flow correction during steady spins did not appear to be as promising as the more complete spin analysis techniques.
8. If wind-tunnel data is not available, it would be preferable to use results from any of the three methods to estimate the angle-of-attack flow correction in a spin than to not apply a correction at all.

APPENDIX

CALCULATION OF FLOW DIRECTION ANGLES

A set of relations may be developed which can be used to calculate the angles of attack and sideslip of an airplane in a steady spin. This method was proposed in reference 15 and is rederived here in a more complete manner. This method utilizes the linear accelerations, angular rates, and the vertical velocity to compute the true angle of attack and true angle of sideslip at the center-of-gravity location of the airplane.

Because some of the measurements are made with respect to the airplane body axes (the linear accelerations and angular rates) and others with respect to the ground axes (the vertical velocity), the relationship between the two axis systems must be determined.

The ground axis system has its origin at the center-of-gravity location of the airplane. The Z_g axis points vertically downward and is aligned with the gravity vector. The X_g axis is in the horizontal plane and points through the spin axis. The Y_g axis is in the horizontal plane and is mutually perpendicular to the X_g and Z_g axes. The ground axis systems turns with the center-of-gravity location of the airplane as the airplane travels in a helical path about the spin axis. Figure 36 shows an instantaneous arrangement of the ground axis system.

The angular velocity of the airplane about the spin axis in the body axis system may be determined from the body angular rates as shown:

$$\bar{\omega} = p \hat{i} + q \hat{j} + r \hat{k}$$

$$|\bar{\omega}| = \sqrt{p^2 + q^2 + r^2}$$

But the spin axis is vertical in the ground axis system, therefore:

$$\bar{\Omega} = |\bar{\Omega}| \mathbf{k}$$

For an equilibrium spin, the resultant force or resultant acceleration vector must be located in the $X_g Z_g$ plane. Figure 37 shows the relationship between the resultant acceleration and resultant rotation vectors. The resultant acceleration may be determined by the measured body linear accelerations:

$$\bar{A} = a_x \hat{i} + a_y \hat{j} + a_z \hat{k}$$

By using the Law of Cosines, the angle between the resultant acceleration and the resultant rotation vectors may be found as follows:

$$|\bar{A} - \bar{\Omega}|^2 = |\bar{A}|^2 + |\bar{\Omega}|^2 - 2|\bar{A}| \cdot |\bar{\Omega}| \cos \sigma$$

$$(\bar{A} - \bar{\Omega}) \cdot (\bar{A} - \bar{\Omega}) = \bar{A} \cdot \bar{A} + \bar{\Omega} \cdot \bar{\Omega} - 2|\bar{A}| \cdot |\bar{\Omega}| \cos \sigma$$

$$\bar{A} \cdot \bar{A} - \bar{A} \cdot \bar{\Omega} - \bar{A} \cdot \bar{\Omega} + \bar{\Omega} \cdot \bar{\Omega} = \bar{A} \cdot \bar{A} + \bar{\Omega} \cdot \bar{\Omega} - 2|\bar{A}| \cdot |\bar{\Omega}| \cos \sigma$$

$$2 \bar{A} \cdot \bar{\Omega} = 2|\bar{A}| \cdot |\bar{\Omega}| \cos \sigma$$

$$\cos \sigma = \frac{\bar{A} \cdot \bar{\Omega}}{|\bar{A}| \cdot |\bar{\Omega}|}$$

$$\cos \sigma = \frac{p(a_x) + q(a_y) + r(a_z)}{|\bar{A}| \cdot |\bar{\Omega}|}$$

Once σ is known, the resultant acceleration vector can be transferred into the ground axis system:

$$|\bar{A}_X| = |\bar{A}| \sin \sigma$$

$$|\bar{A}_Z| = |\bar{A}| \cos \sigma$$

Since the airplane is in equilibrium, the aerodynamic acceleration in the vertical direction must be equal and opposite to the acceleration of gravity, in other words:

$$|\bar{A}_Z| = 1g$$

The center of gravity of the airplane exhibits a circular motion in the X_g Y_g plane; thus the velocity in this plane is in the Y_g direction only (i.e., $U = 0$). Also, the aerodynamic acceleration in the X_g direction must be equal to the centrifugal acceleration in order for the airplane to be in equilibrium:

$$|\bar{A}_X| g = \bar{A}_C$$

$$\bar{A}_C = \frac{V^2}{R_S}$$

$$V = |\bar{\Omega}| R_S$$

$$\bar{A}_C = \frac{|\bar{\Omega}|^2 R_S^2}{R_S} = |\bar{A}_X| g$$

$$R_S = \frac{|\bar{A}_X| g}{|\bar{\Omega}|^2}$$

$$\bar{A}_C = \frac{V |\bar{\Omega}| R_S}{R_S} = |\bar{A}_X| g$$

$$V |\bar{\Omega}| = |\bar{A}_X| g$$

$$v = \frac{|A_x| g}{|\bar{\Omega}|}$$

$$|\bar{v}| = \sqrt{u^2 + v^2 + w^2}$$

$$w = -h, u = 0$$

$$|\bar{v}| = \sqrt{v^2 + (-h)^2}$$

$$\delta = \tan^{-1} \left(\frac{v}{-h} \right)$$

Next, we define a vector, \bar{x}'_g , which is parallel to the x_g axis and intersects the resultant acceleration vector at unit distance from origin (see figure 37):

$$\bar{x}'_g = \frac{\bar{A}}{|\bar{A}|} - \cos \sigma \frac{\bar{\Omega}}{|\bar{\Omega}|}$$

The direction components of \bar{x}'_g in the body axes are:

$$i = \frac{a_x}{|\bar{A}|} - \cos \sigma \frac{p}{|\bar{\Omega}|}$$

$$j = \frac{a_y}{|\bar{A}|} - \cos \sigma \frac{q}{|\bar{\Omega}|}$$

$$k = \frac{a_z}{|\bar{A}|} - \cos \sigma \frac{r}{|\bar{\Omega}|}$$

$$|\bar{x}'_g| = \sqrt{|i|^2 + |j|^2 + |k|^2}$$

The Y_g axis is mutually perpendicular to the X_g and Z_g axes and its direction may be found by the definition of orthogonality:

$$\hat{I} \cdot \hat{J} = 0$$

$$\hat{J} \cdot \hat{J} = 1$$

$$\hat{K} \cdot \hat{J} = 0$$

The direction cosines of the Y_g axis in the body axes are found by the solution of the following direction cosine equation:

$$\begin{bmatrix} l_X & m_X & n_X \\ l_Y & m_Y & n_Y \\ l_Z & m_Z & n_Z \end{bmatrix} \begin{bmatrix} l_Y \\ m_Y \\ n_Y \end{bmatrix} = \begin{bmatrix} 0 \\ 1 \\ 0 \end{bmatrix}$$

Using Cramer's rule of determinants

$$l_Y = - \begin{vmatrix} m_X & n_X \\ m_Z & n_Z \end{vmatrix} = m_Z n_X - m_X n_Z$$

$$l_Y = \frac{q}{|\bar{\Omega}|} \frac{k}{|\bar{x}'_g|} - \frac{j}{|\bar{x}'_g|} \frac{r}{|\bar{\Omega}|}$$

$$m_Y = \begin{vmatrix} l_X & n_X \\ l_Z & n_Z \end{vmatrix} = l_X n_Z - l_Z n_X$$

$$m_Y = \frac{i}{|\bar{X}'_g|} \frac{r}{|\bar{\Omega}|} - \frac{p}{|\bar{\Omega}|} \frac{k}{|\bar{X}'_g|}$$

$$n_Y = - \begin{vmatrix} l_X & m_X \\ l_Z & m_Z \end{vmatrix} = l_Z m_X - l_X m_Z$$

$$n_Y = \frac{p}{|\bar{\Omega}|} \frac{j}{|\bar{X}'_g|} - \frac{i}{|\bar{X}'_g|} \frac{q}{|\bar{\Omega}|}$$

Next the direction cosines in the ground axis system are determined.

The direction cosines of the flight path are:

$$l'_V = 0$$

$$m'_V = \pm \sin \delta \quad \begin{array}{l} - \text{ for right spins} \\ + \text{ for left spins} \end{array}$$

$$n'_V = \cos \delta$$

The direction cosines of the Y_b body axis are:

$$l'_Y = m_X$$

$$m'_Y = m_Y$$

$$n'_Y = \pm m_Z \quad \begin{array}{l} + \text{ for right spins} \\ - \text{ for left spins} \end{array}$$

The direction of the cosines of the X_b body axis are:

$$l'_X = l_X$$

$$m'_X = l_Y$$

$$n'_X = \pm l_Z \quad \begin{array}{l} + \text{ for right spins} \\ - \text{ for left spins} \end{array}$$

The relationship between a line and a plane is used to find the ground flight path components in the body system of axes:

$$\sin \beta_t = \frac{v}{|\bar{V}|} = (\ell'_v \ell'_y + m'_v m'_y + n'_v n'_y)$$

$$\sin \beta_t = \frac{\pm v}{|\bar{V}|} \left(\frac{i}{|\bar{X}'_g|} \frac{r}{|\bar{\Omega}|} - \frac{p}{|\bar{\Omega}|} \frac{k}{|\bar{X}'_g|} \right) + \frac{(-h) \pm q}{|\bar{V}| |\bar{\Omega}|}$$

$$\cos \mu = \frac{u}{|\bar{V}|} = (\ell'_v \ell'_x + m'_v m'_x + n'_v n'_x)$$

$$\cos \mu = \frac{\pm v}{|\bar{V}|} \left(\frac{q}{|\bar{\Omega}|} \frac{k}{|\bar{X}'_g|} - \frac{j}{|\bar{X}'_g|} \frac{r}{|\bar{\Omega}|} \right) + \frac{(-h) \pm p}{|\bar{V}| |\bar{\Omega}|}$$

$$\cos \beta_t = \frac{\sqrt{u^2 + w^2}}{|\bar{V}|}, \quad \cos \alpha_t = \frac{u}{\sqrt{u^2 + w^2}}$$

$$\cos \alpha_t = \frac{\cos \mu}{\cos \beta_t}$$

$$\alpha_t = \cos^{-1} \left(\frac{\cos \mu}{\cos \beta_t} \right)$$

REFERENCES

1. Kershner, David: Miniature Flow-Direction and Airspeed Sensor for Airplane and Radio-Controlled Models in Spin Studies. NASA TP 1467, 1979.
2. Alford, William J., Jr.: Theoretical and Experimental Investigation of the Subsonic-Flow Fields Beneath Swept and Unswept Wings with Tables of Vortex-Induced Velocities. NASA TN 3738, 1956.
3. Sliwa, Steven M.: A Study of Data Extraction Techniques for Use in General Aviation Aircraft Spin Research. Master's Thesis, George Washington University, September 1978.
4. Gracey, William: Summary of Methods of Measuring Angle of Attack on Aircraft. NASA TN 4351, 1958.
5. Ribner, Herbert S.: Notes on the Propeller and Slipstream in Relation to Stability. NACA WR L-25, 1944.
6. Milne-Thomson, L. M.: Theoretical Aerodynamics. Fourth Ed. Dover Publications, Inc., 1966.
7. Bowman, James S.; Stough, H. Paul; Burk, Sanger M.; and Patton, James M.: Correlation of Model and Airplane Spin Characteristics for a Low-Wing General Aviation Airplane. AIAA Paper No. 78-1977, August 1978.
8. Moul, Thomas M.: Wind-Tunnel Investigation of the Flow Correction for a Model-Mounted Angle of Attack Sensor at Angles of Attack From -10° to 110° . NASA TM 80189, 1979.
9. Moul, Thomas M.; and Taylor, Lawrence W., Jr.: Determination of an Angle of Attack Sensor Correction for a General Aviation Airplane at Large Angles of Attack as Determined from Wind Tunnel and Flight Tests. AIAA Paper No. 80-1845, August 1980.
10. O'Bryan, Thomas C.; Gcode, Maxwell W.; Gregory, Frederick D.; and Mayo, Marna H.: Description of an Experimental (Hydrogen Peroxide) Rocket System and Its Use in Measuring Aileron and Rudder Effectiveness of a Light Airplane. NASA TP 1647, 1980.
11. Staff of the Langley Research Center: Exploratory Study of the Effects of Wing Leading-Edge Modifications on the Stall/Spin Behavior of a Light General Aviation Airplane. NASA TP 1589, 1979.
12. Mulcay, William J.; and Rose, Robert A.: Rotary-Balance Data for a Typical Single-Engine General Aviation Design for an Angle-of-Attack Range of 8° to 90° ; I - Low-Wing Model C. NASA CR 3200, 1980.

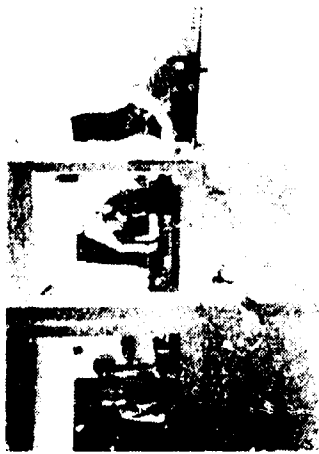
13. Etkin, Bernard: Dynamics of Atmospheric Flight. John Wiley and Sons, Inc., 1972.
14. Gainer, Thomas G.; and Hoffman, Sherwood: Summary of Transformation Equations and Equations of Motion Used in Free-Flight and Wind-Tunnel Data Reduction and Analysis. NASA SP-3070, 1972.
15. Soulé, Hartley A.; and Scudder, Nathan F.: A Method of Flight Measurement of Spins. NACA Report No. 377, 1931.
16. Newsom, William A., Jr.; Satran, Dale R.; and Johnson, Joseph L., Jr.: Effects of Wing Leading-Edge Modifications on a Full-Scale, Low-Wing General Aviation Airplane--Wind-Tunnel Investigation of High Angle of Attack Aerodynamic Characteristics. NASA TP 2011, 1982.
17. Hoerner, Sigward F.: Fluid-Dynamic Lift. Hoerner Fluid Dynamics, 1975.

TABLE I.- CHARACTERISTICS OF RESEARCH AIRPLANE

Maximum gross mass (normal category), kg (lbm)	1110 (2450)
Engine kW (hp)	130 (180)
Propeller diameter, m (ft)	1.93 (6.33)
Length, m (ft)	7.84 (25.73)
Height, m (ft)	2.50 (8.20)
Wing airfoil	NACA 63 ₂ A415
Wing span, m (ft)	9.98 (32.75)
Wing area, m ² (ft ²)	13.56 (146)
Wing chord, m (ft)	1.34 (4.39)
Wing mean aerodynamic chord, m (ft)	1.34 (4.39)
Aspect ratio	7.35
Dihedral, deg	6.5
Aileron span, m (ft)	1.64 (5.38)
Aileron area (each), m ² (ft ²)	0.64 (6.93)
Aileron chord, m (ft)	0.39 (1.29)
Vertical tail airfoil	NACA 63 ₁ A012 modified
Vertical tail area, m ² (ft ²)	1.36 (14.6)
Rudder area, m ² (ft ²)	0.43 (4.62)
Horizontal tail airfoil	NACA 63 ₁ A012 modified
Horizontal tail area, m ² (ft ²)	2.51 (27.0)
Tail length (quarter chord of wing to quarter chord of vertical tail), m (ft)	4.14 (13.6)
Location of flow direction and velocity sensor pivot point:	
Outboard from airplane center line, m (ft)	4.41 (14.47)
Forward from leading edge of wing, m (ft)	1.06 (3.49)
Maximum control deflections:	
Ailerons, deg	20 up, 10 down
Elevator, deg	15 up, 2 down
Rudder, deg	25 right, 25 left

TABLE II.- MEASUREMENT LIST FOR RESEARCH AIRPLANE

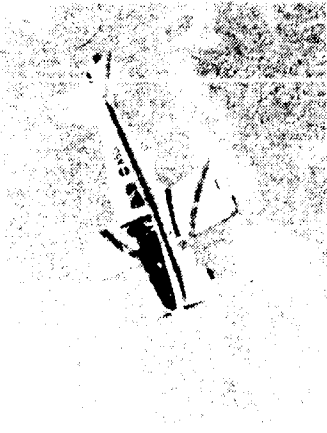
Measurement	Range
Airspeed (right and left), m/sec (mph)	0 to 89.4 (0 to 200)
Angle of attack (right and left), deg	-30 to 150
Angle of sideslip (right and left), deg	±60
Altitude, m (ft)	-150 to 2896 (-500 to 9500)
X-axis acceleration, g units	±1
Y-axis acceleration, g units	±1
Z-axis acceleration, g units	-6 to 3
Pitch rate, deg/sec	±100
Roll rate, deg/sec	±290
Yaw rate, deg/sec	±290
Pitch attitude, deg	±90
Roll attitude, deg	±180
Yaw attitude, deg	±180
Stabilator deflector, deg	-16 to 3
Aileron deflection (right and left), deg	23 up to 10 down
Rudder deflection, deg	±30
Trim tab deflection, deg	-18 to 13
Flap deflection, deg	0 to 35
Throttle, percent	0 to 100
Longitudinal wheel force, N (lb)	±445 (±100)
Lateral wheel force, N (lb)	±156 (±35)
Rudder pedal force, N (lb)	±667 (±150)
Engine speed, rpm	0 to 2900
Rocket chamber pressure (right and left), MPa (psi) ..	0 to 2.07 (0 to 300)
Rate of climb, m/sec (ft/min)	±10.2 (±2000)
Total temperature, °C (°F)	-18 to 38 (0 to 100)
Impact pressure, kPa (psi)	0 to 3.45 (0 to .5)



SPIN TUNNEL



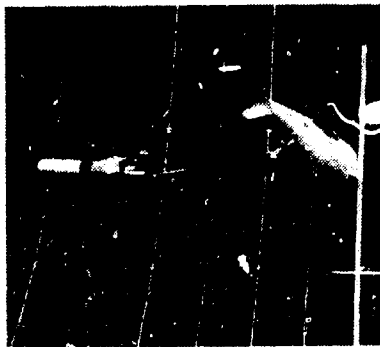
RADIO-CONTROLLED MODELS



FLIGHT TESTS



FULL-SCALE WIND-TUNNEL TESTS



ROTARY-BALANCE TESTS



ANALYTICAL STUDIES

Figure 1.- Scope of the NASA-Langley stall/spin research program.

ORIGINAL PAGE IS
OF POOR QUALITY

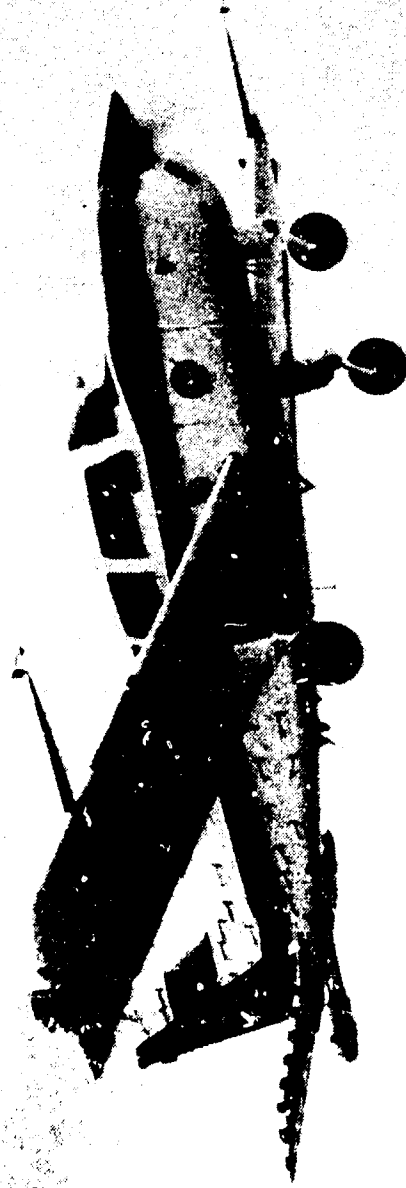


Figure 2.- Spin research airplane in flight.

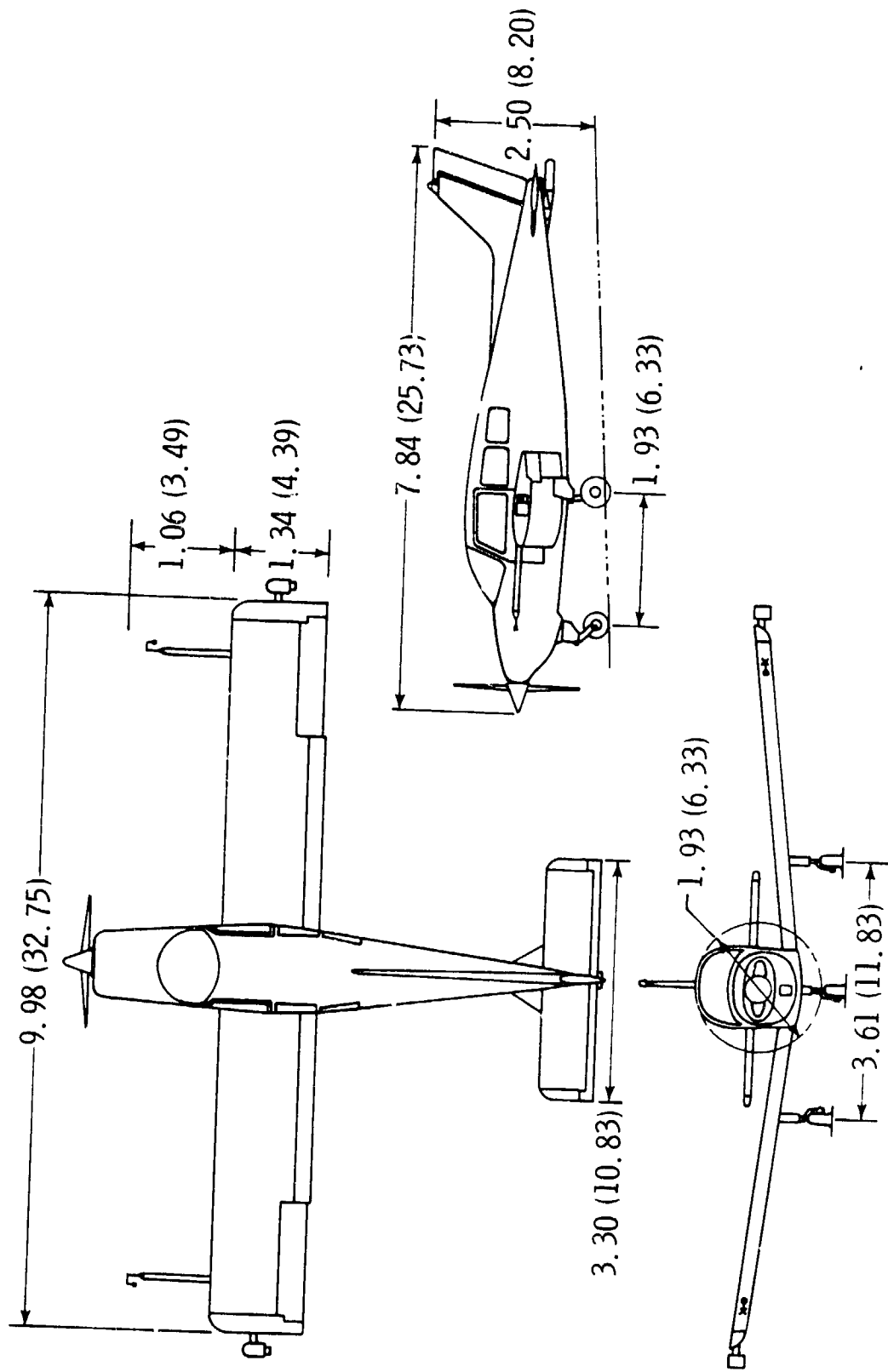
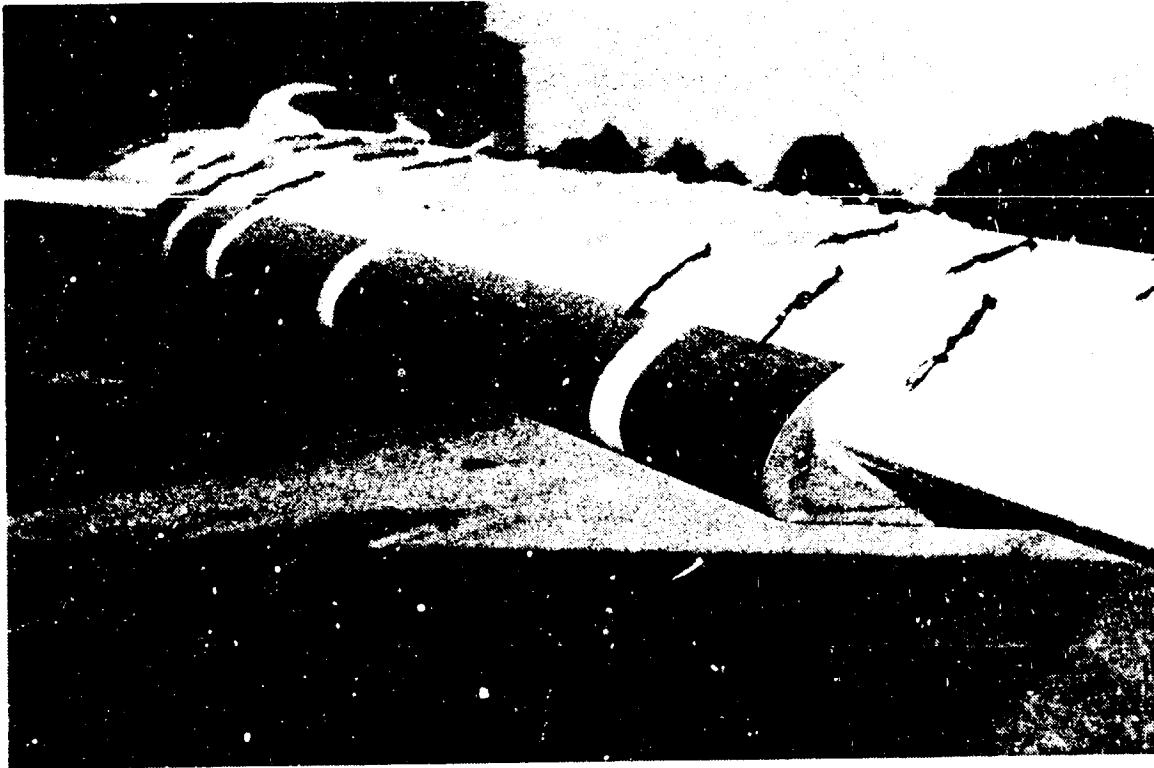


Figure 3.- Three-view drawing of spin research airplane. Dimensions in meters (feet).



OF FOUR

— LEADING EDGE DROOP AIRFOIL

- - - UNMODIFIED AIRFOIL



Figure 4.- Wing leading-edge droop modification.

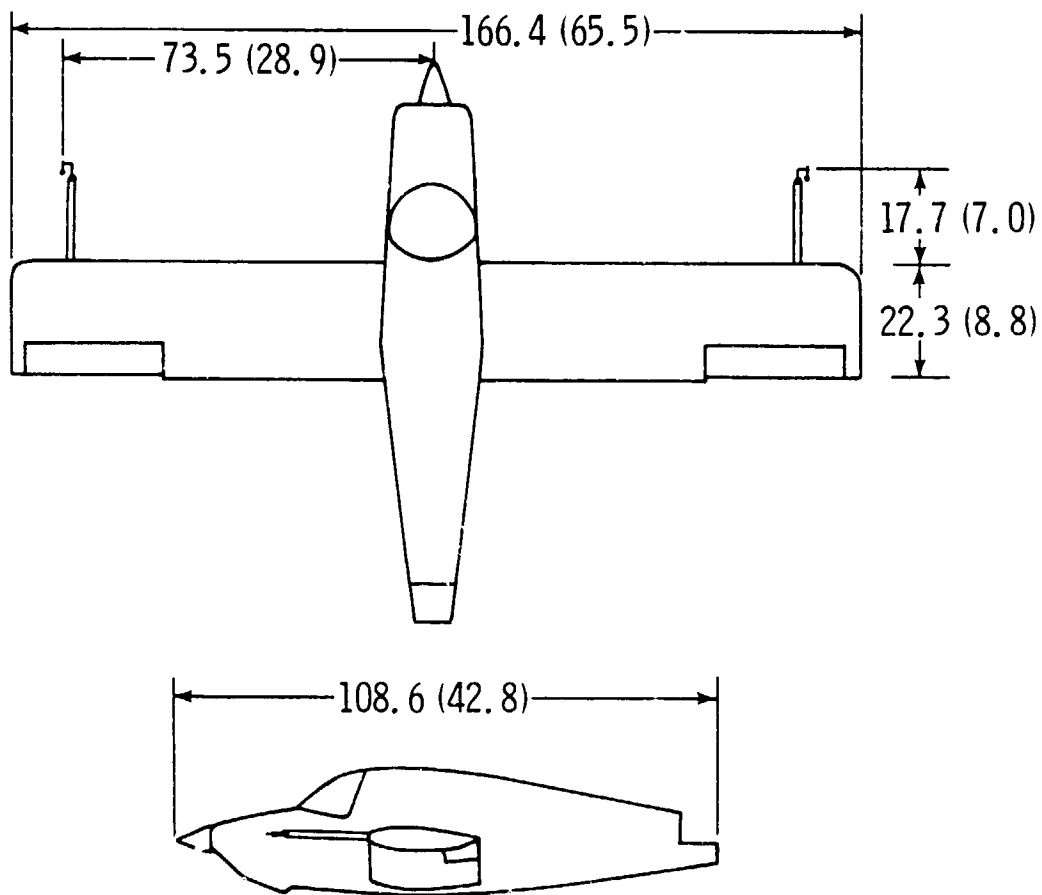


Figure 5.- Dimensions of the 1/6-scale model in centimeters (inches).

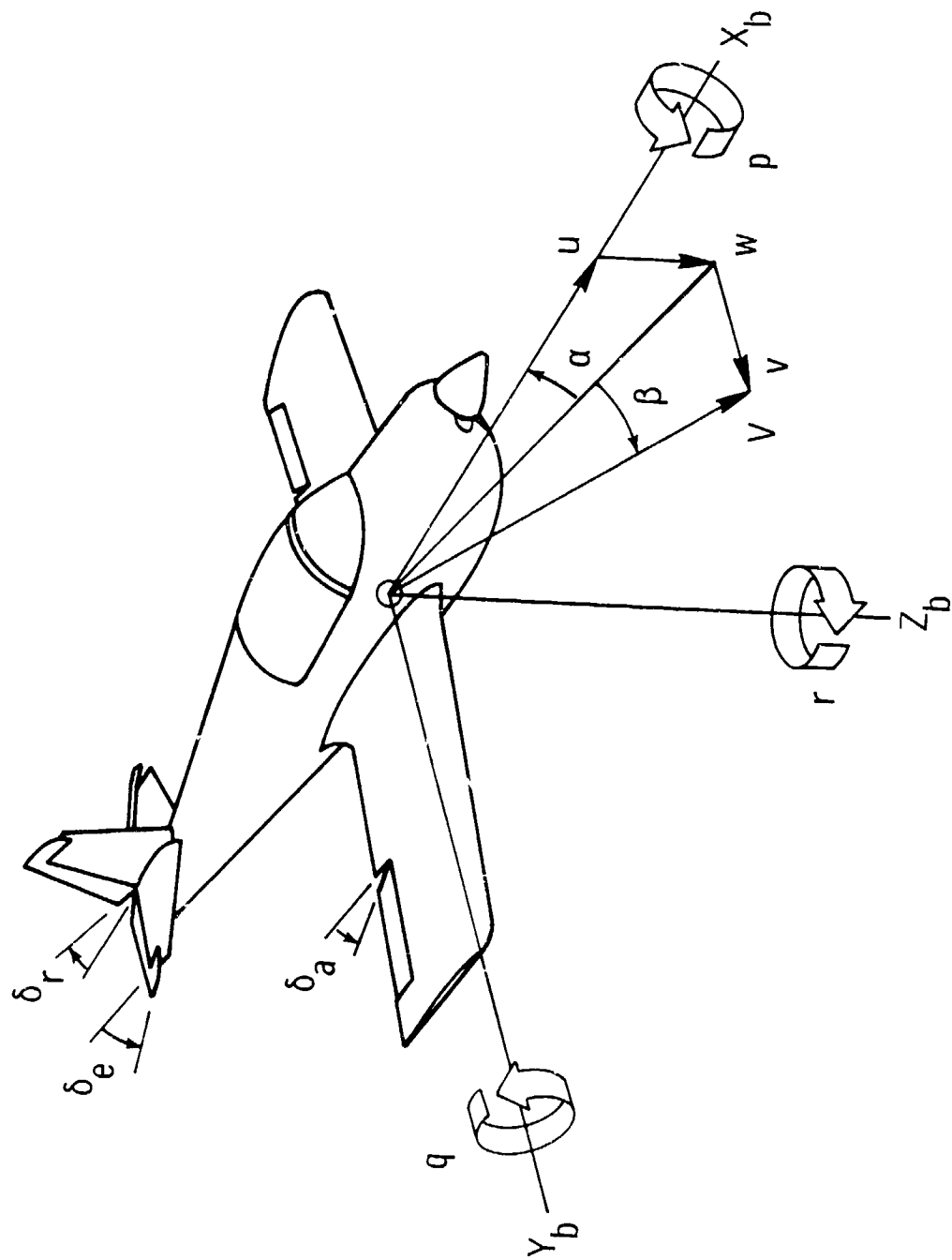
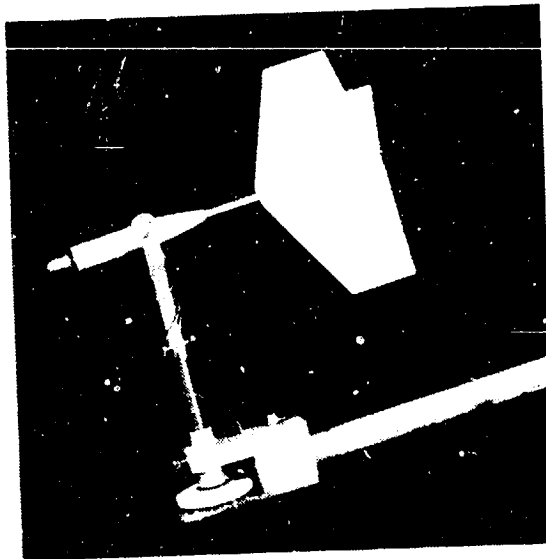
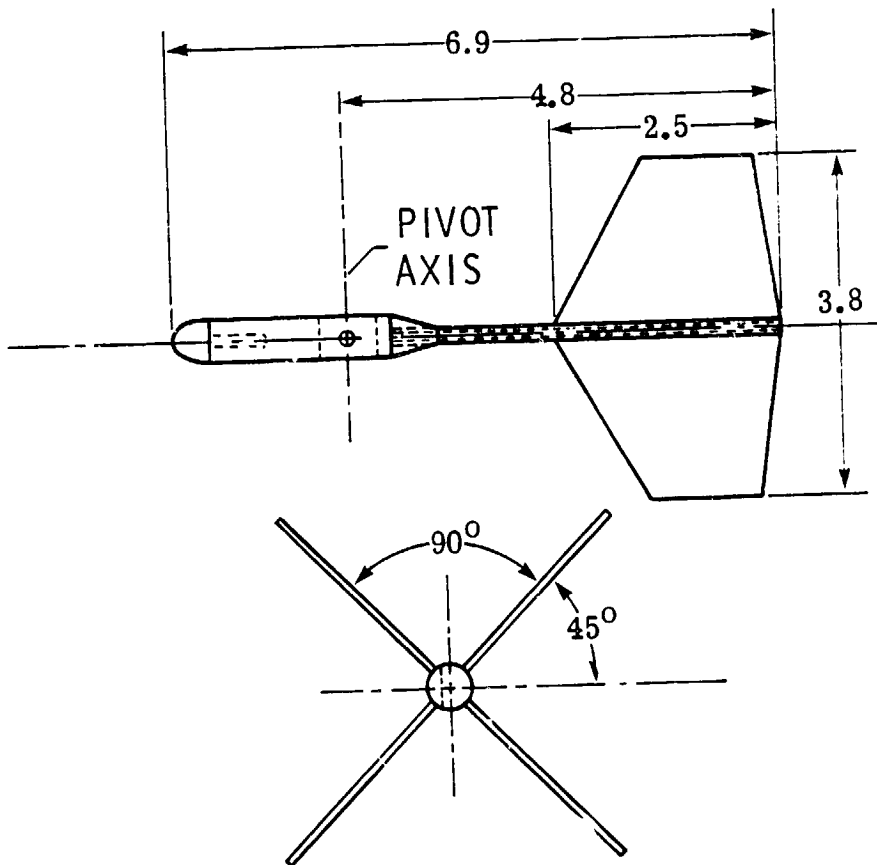


Figure 6.- Definition of body axis system. Arrows indicate positive direction of quantities.

ORIGINAL PAGE IS
OF POOR QUALITY



(a) Photograph of the flow direction sensor.



(b) Dimensions (in cm) of the flow direction sensor.

Figure 7.- Flow direction sensor used in the wind-tunnel tests.

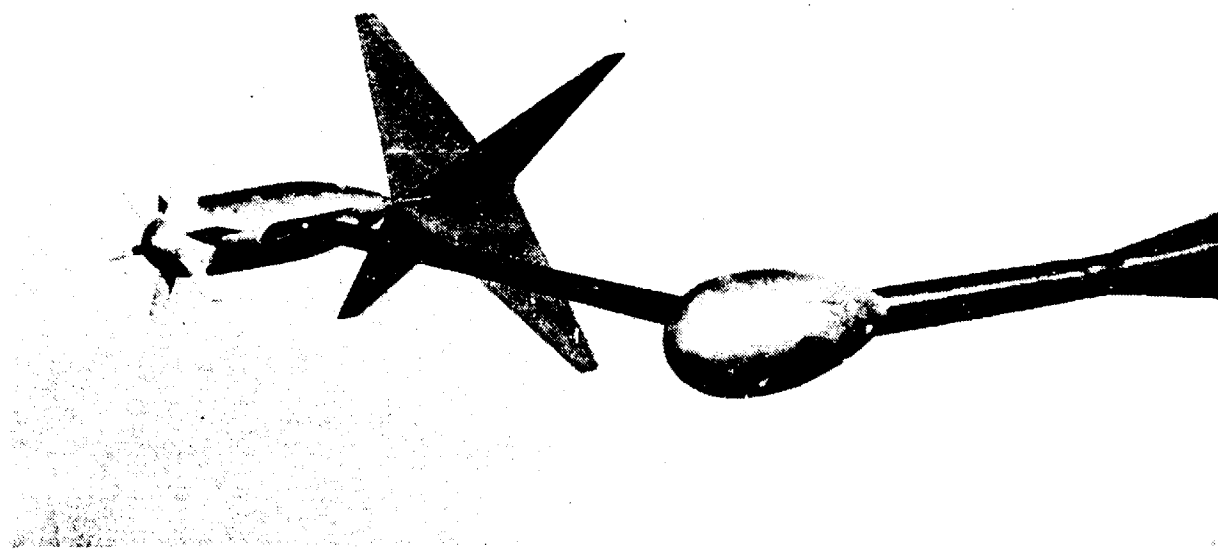


Figure 8.- Flow direction and velocity sensor used in the flight tests.

100-100-00000
OF FOUR QUARTS

GENERAL VIEW
OF POOR QUALITY

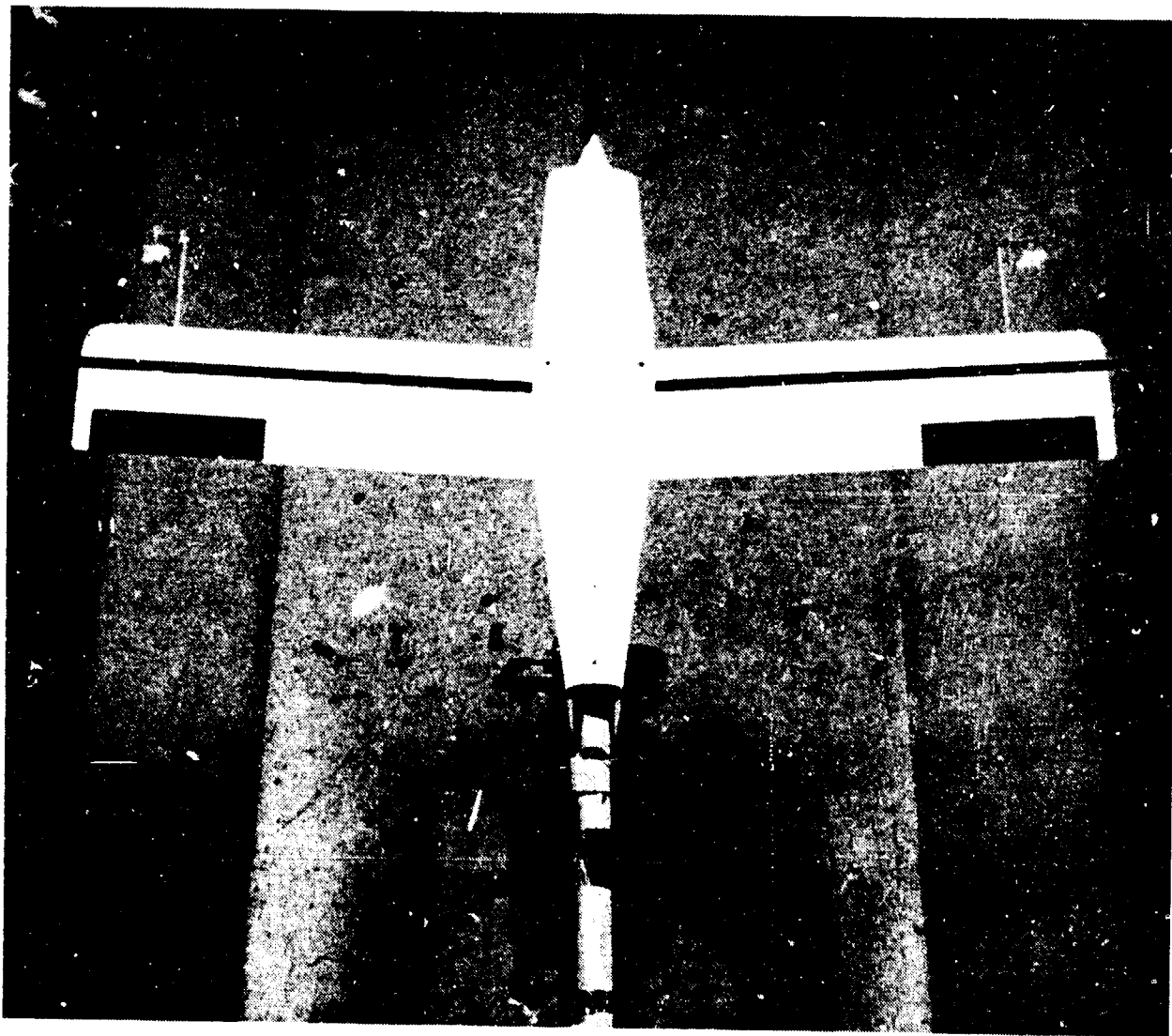


Figure 9.- Model mounted in the 12-foot low-speed wind tunnel.

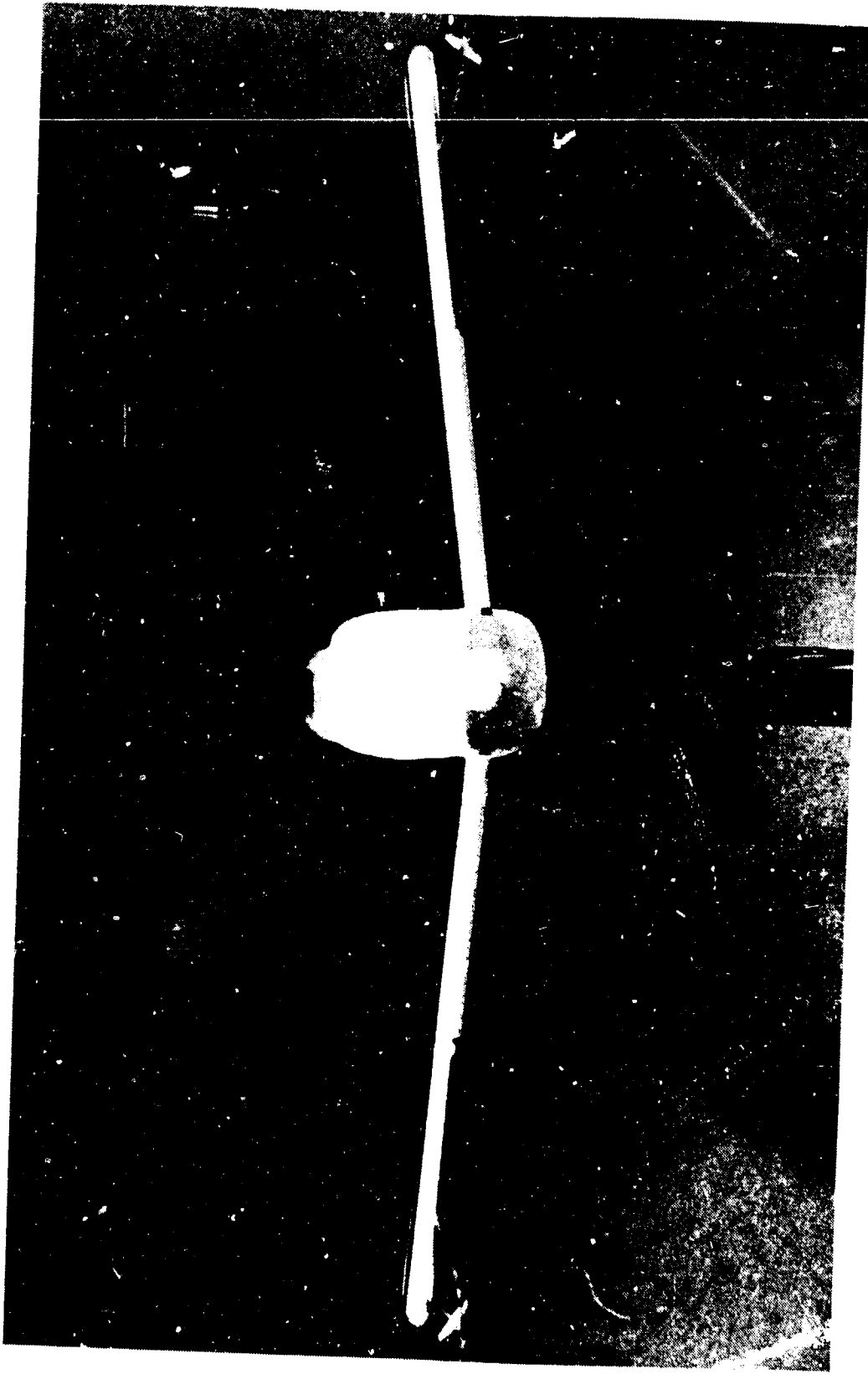
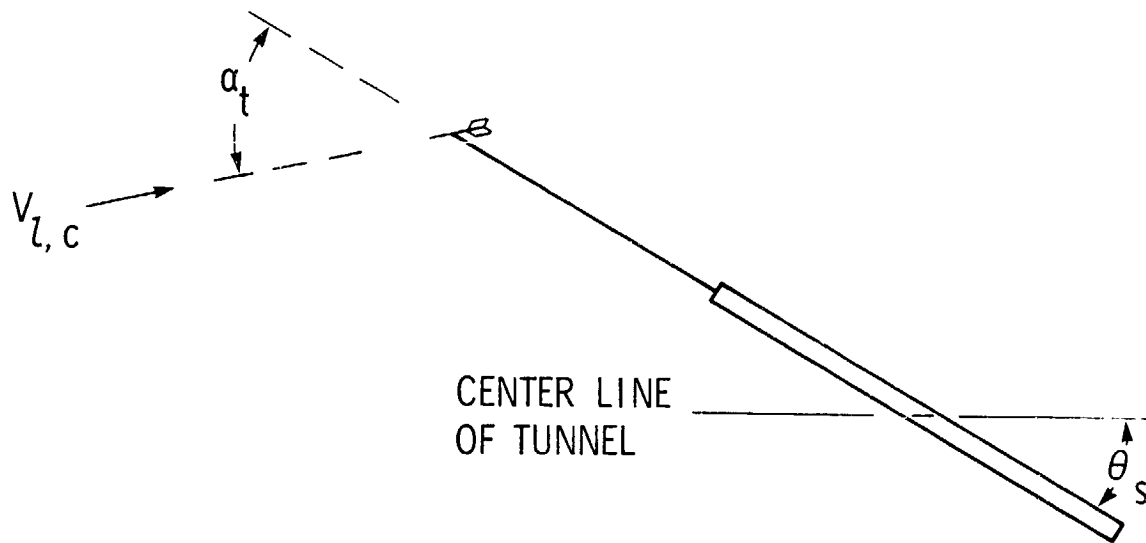
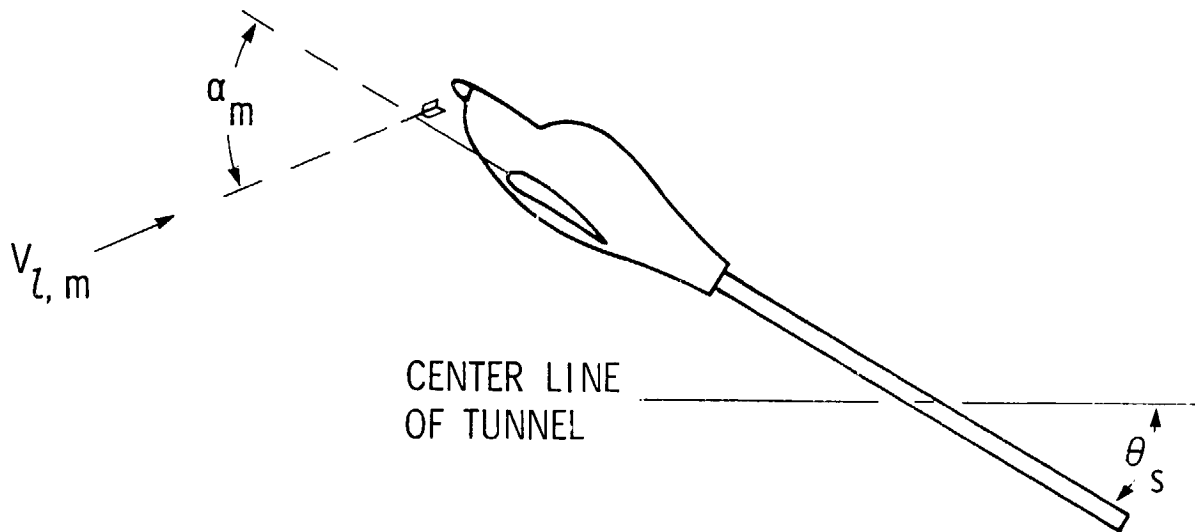


Figure 10.- Model with the outboard leading-edge droop modification applied to the wings.



(a) TUNNEL FLOW CALIBRATION



(b) FLOW DIRECTION MEASUREMENT

Figure 11.- Definition of the angles measured to determine the angle-of-attack flow correction.

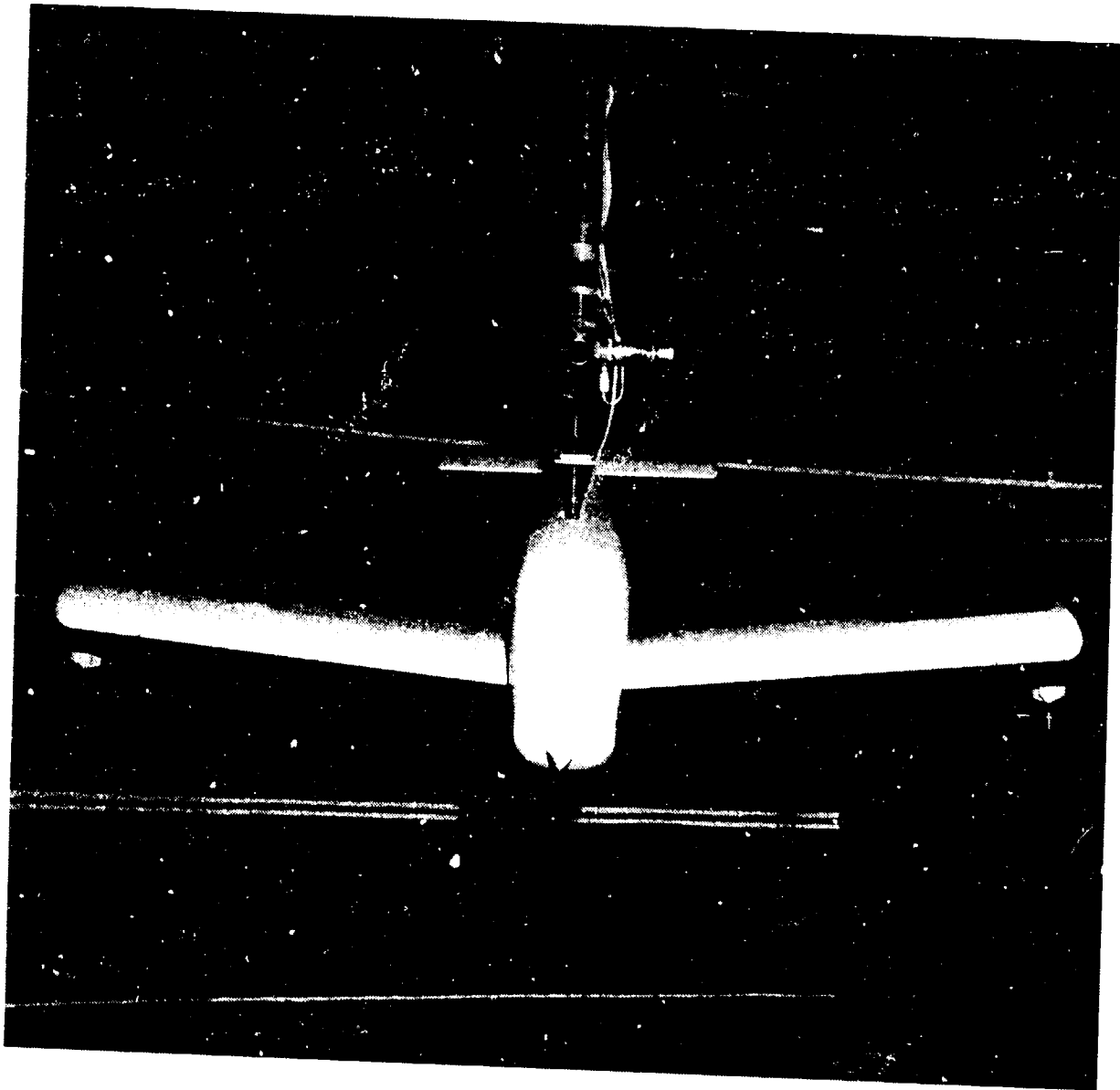
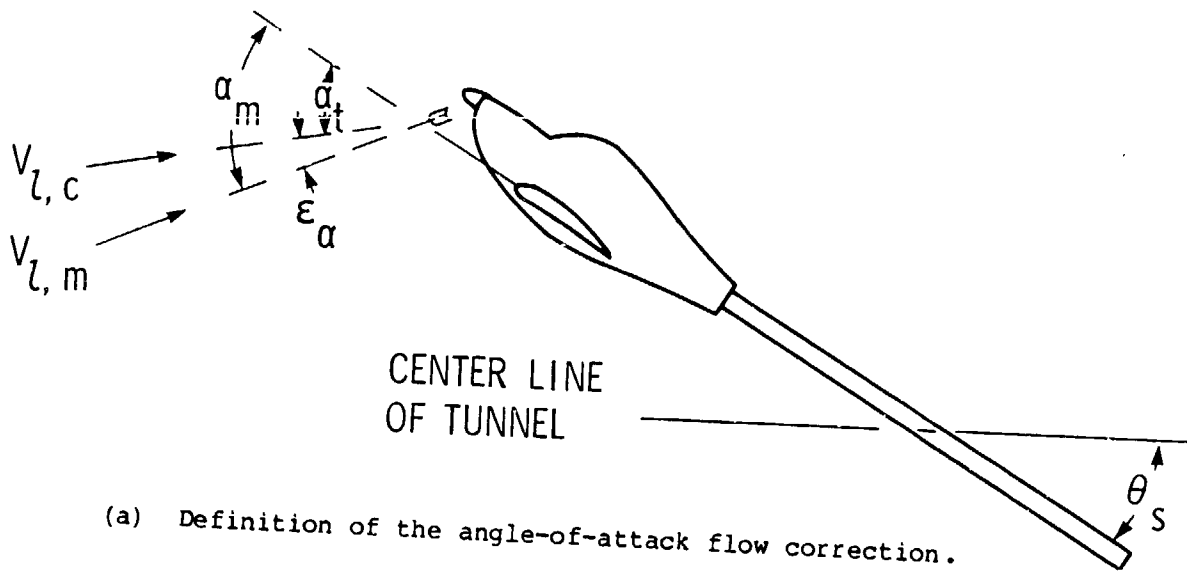
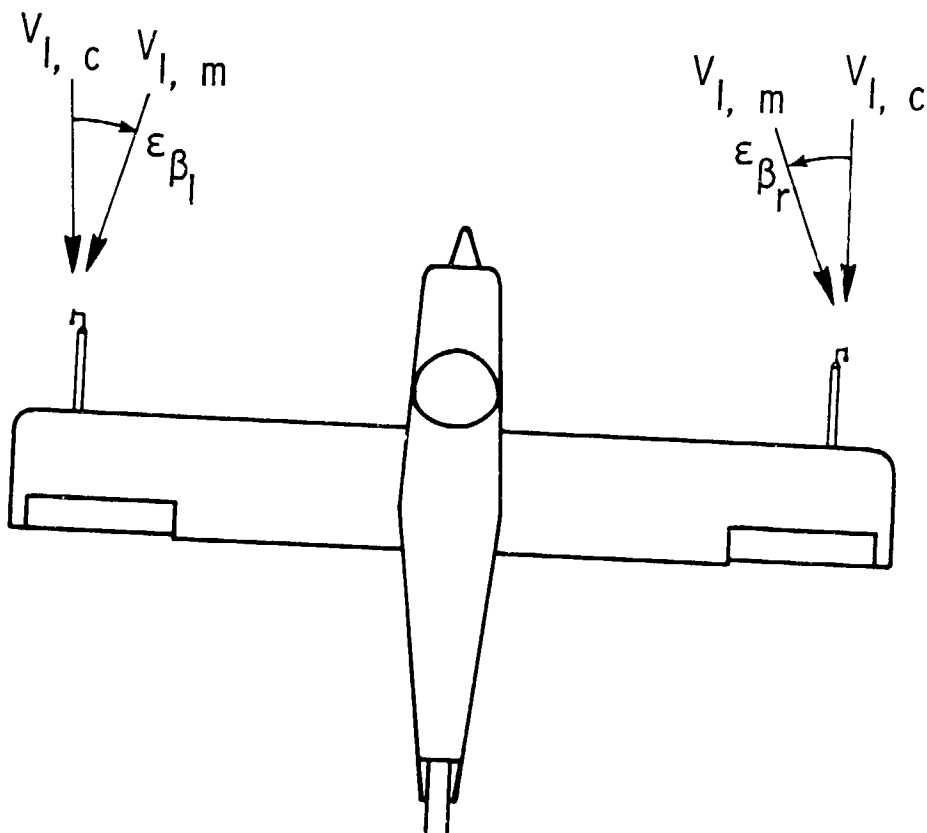


Figure 12.- Model mounted on the rotary-balance apparatus in the spin tunnel.



(a) Definition of the angle-of-attack flow correction.



(b) Definition of the angle-of-sideslip flow correction.

Figure 13.- Definition of the angle-of-attack and angle-of-sideslip flow correction.

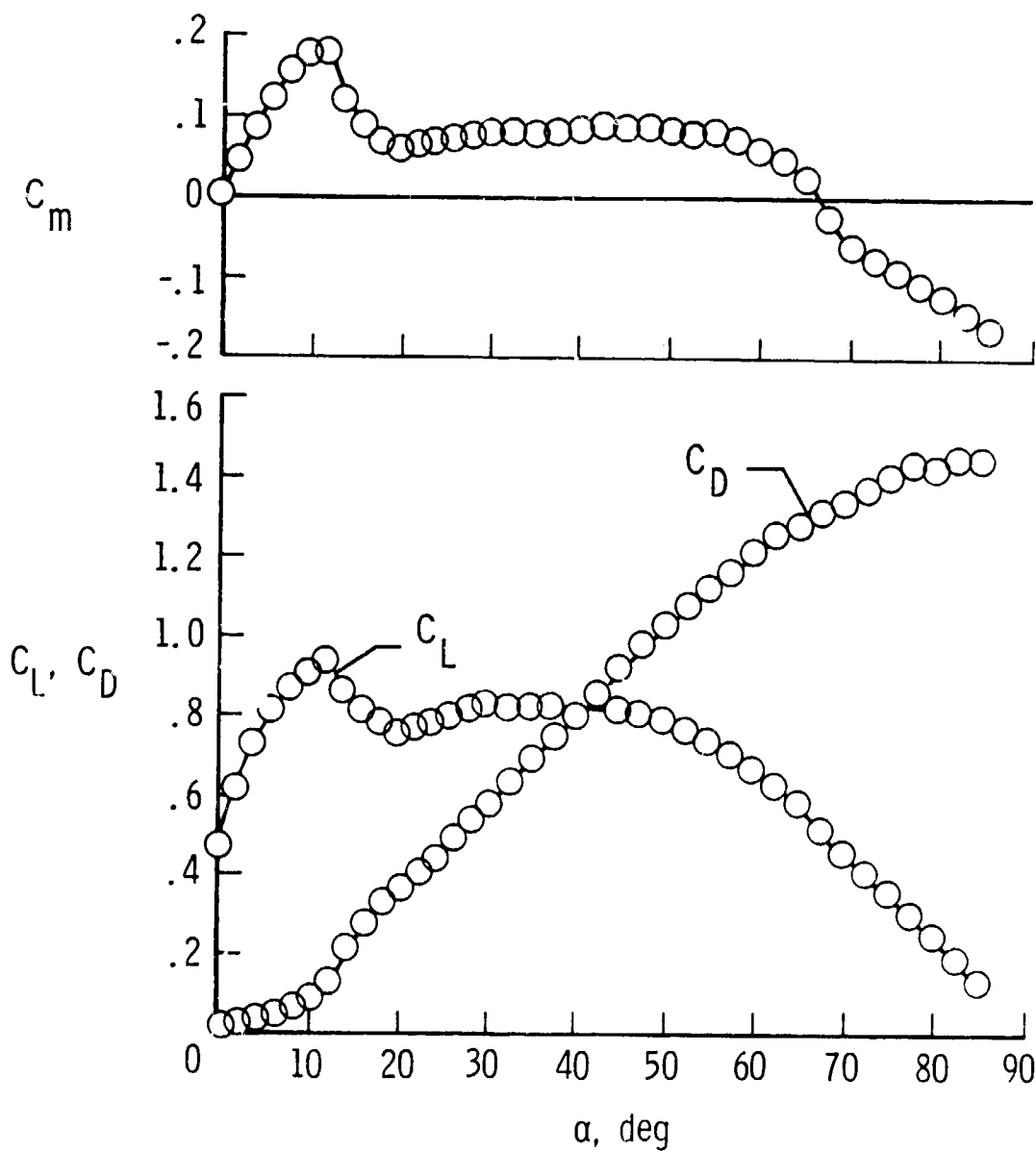


Figure 14.- Longitudinal force and moment data for the model.

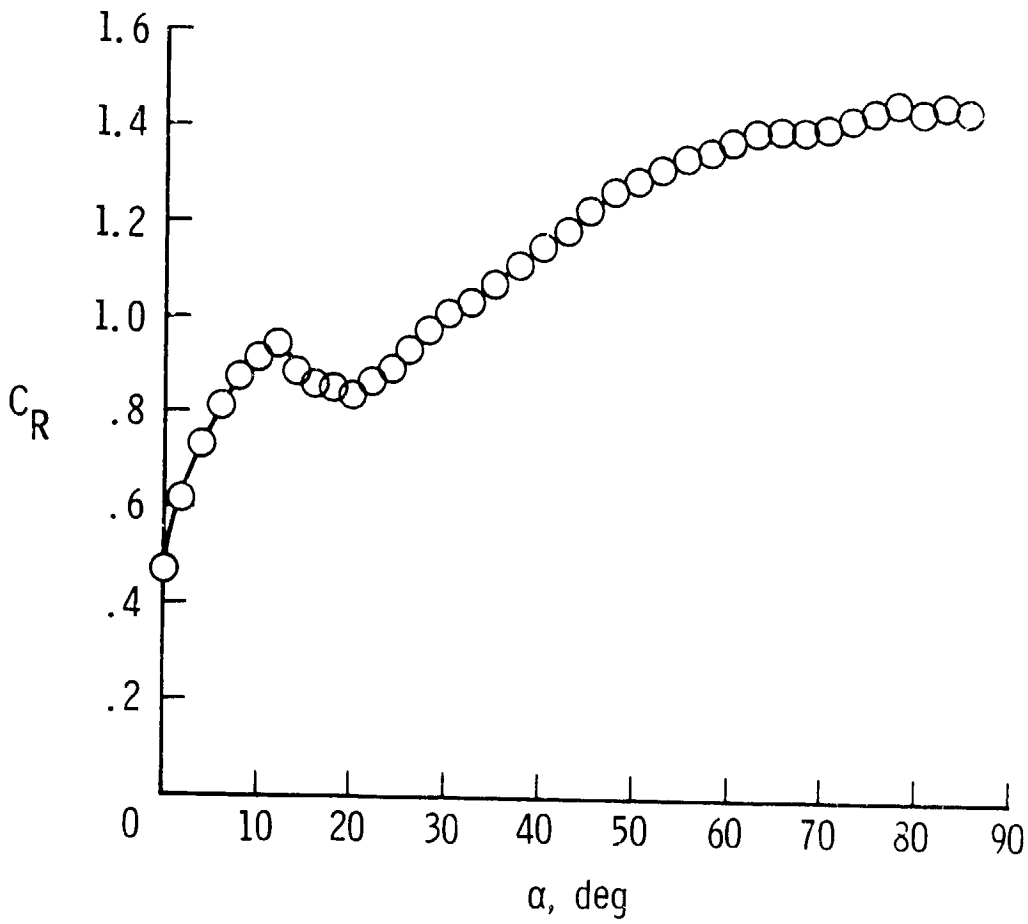


Figure 15.- Resultant-force coefficient data for the model.

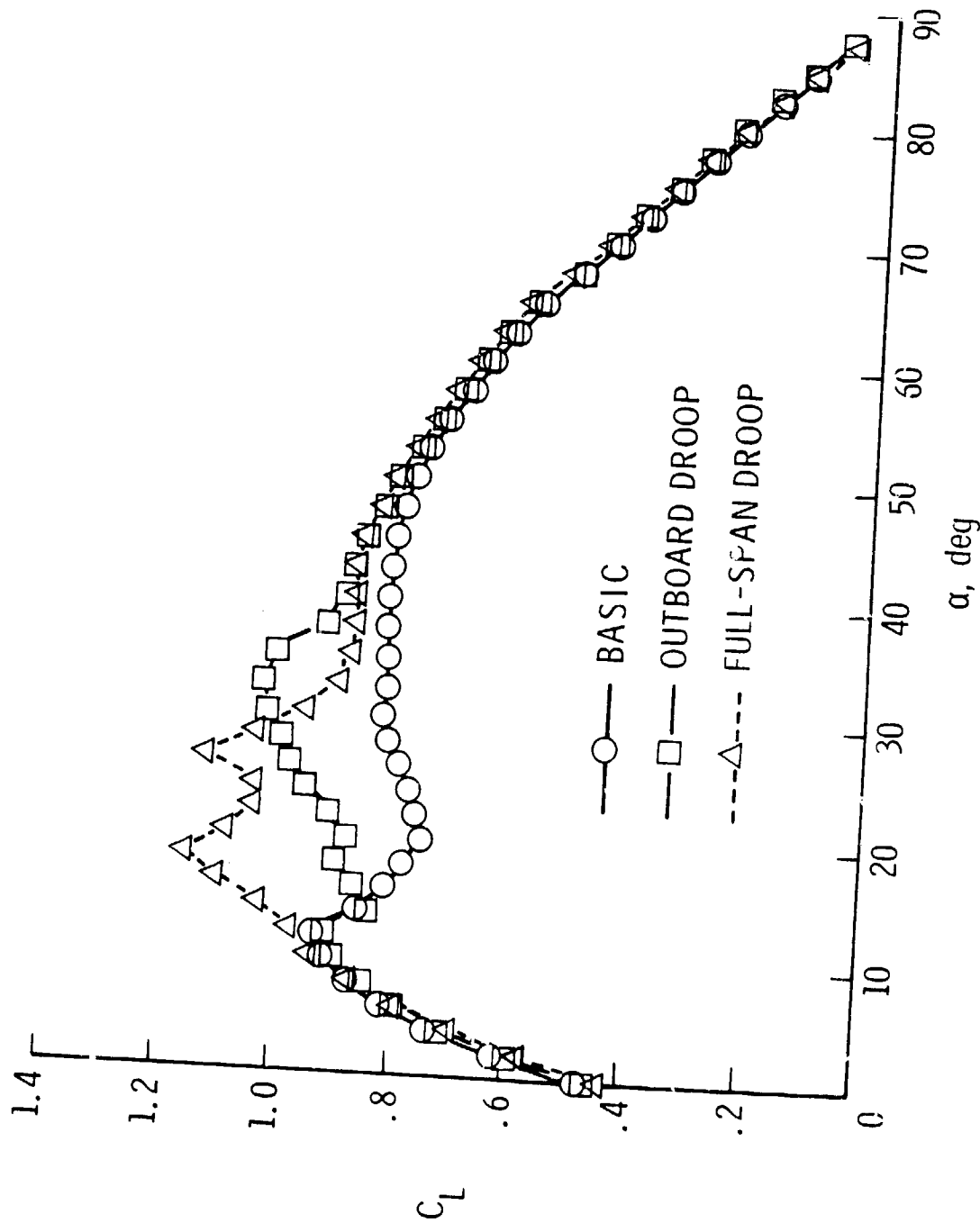


Figure 16.- The effect of leading-edge modifications on the lift coefficient of the model.

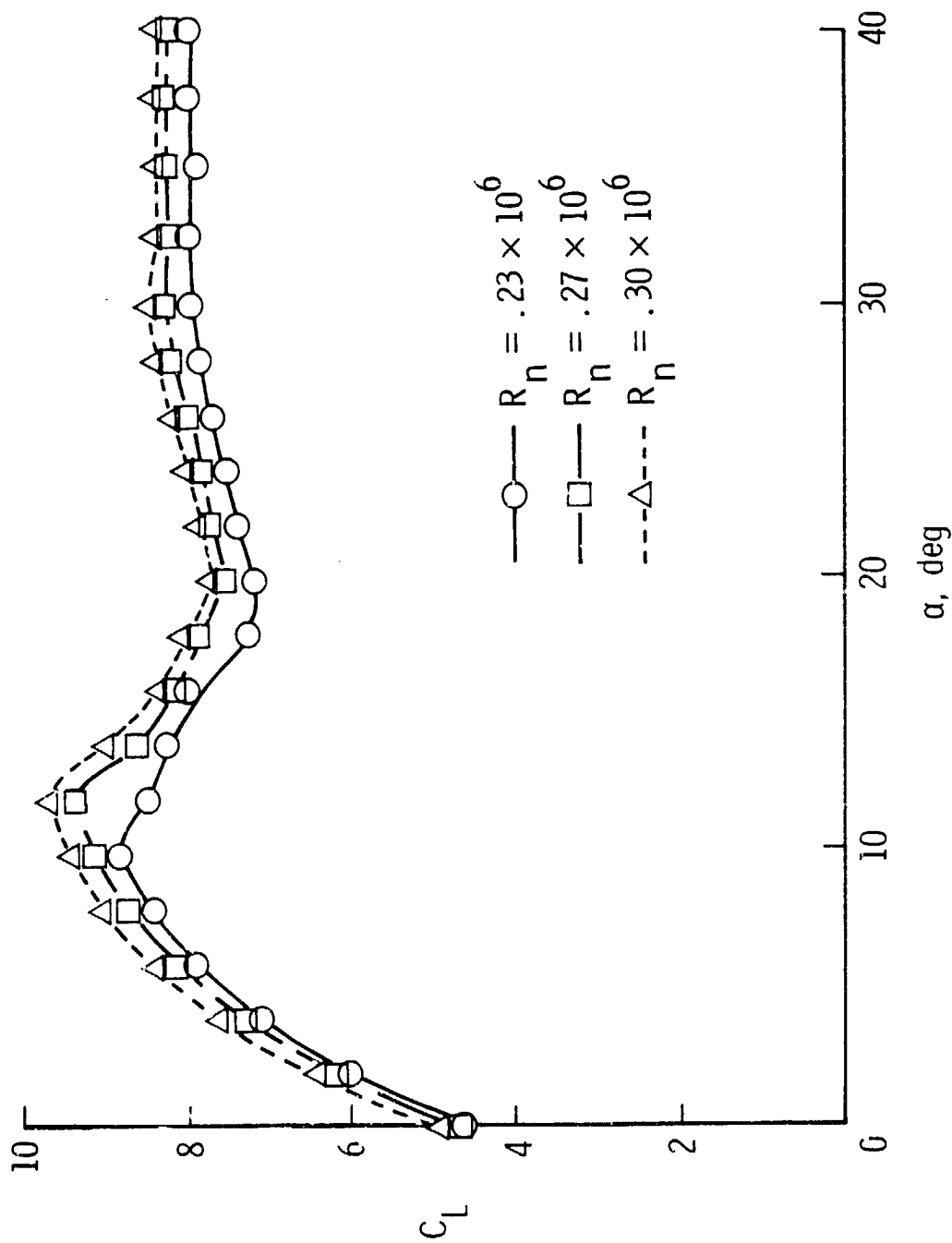


Figure 17.- The effect of the Reynolds number on the lift coefficient of the model.

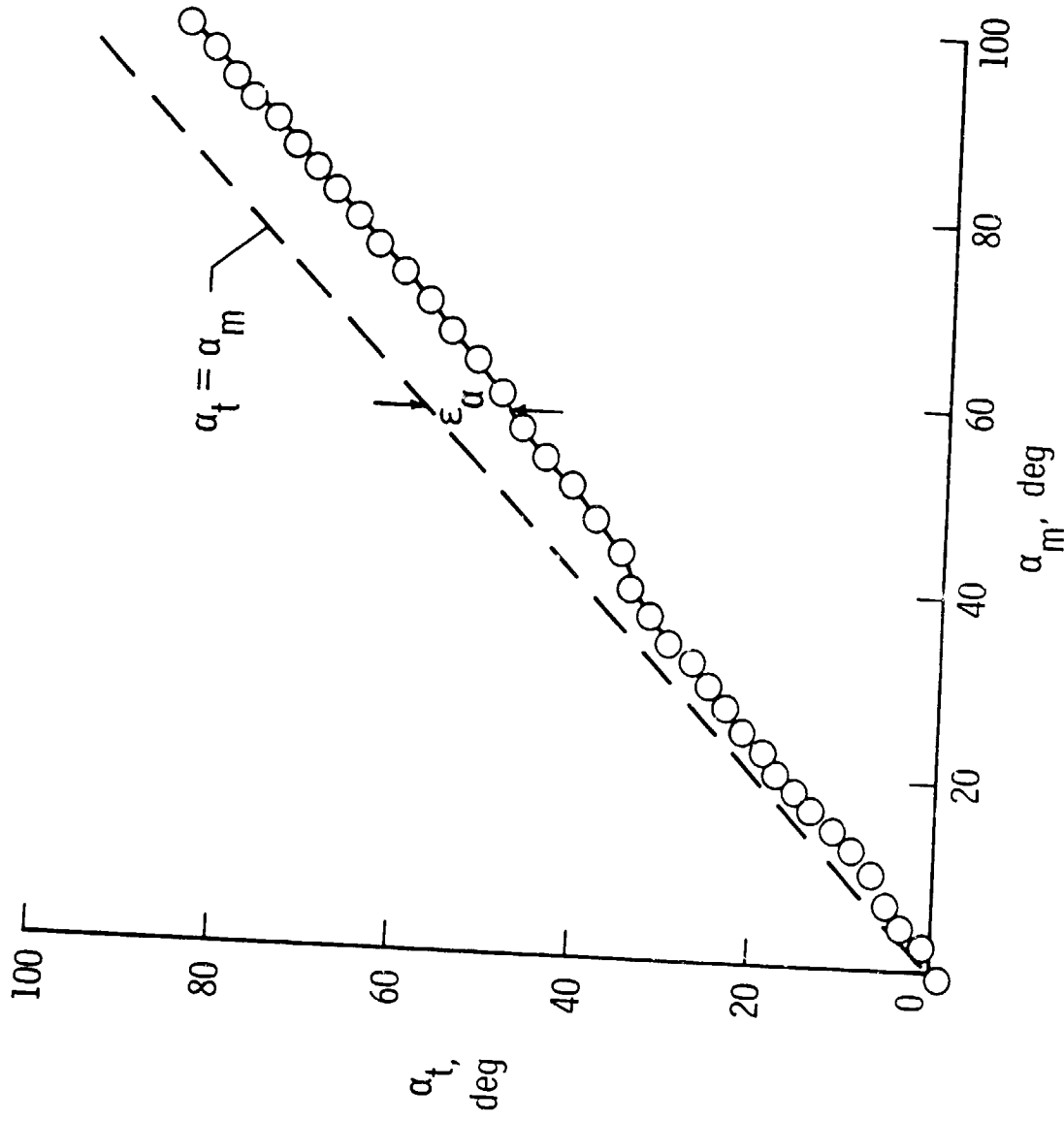


Figure 18.- The true versus the measured angle of attack from the static wind-tunnel tests.

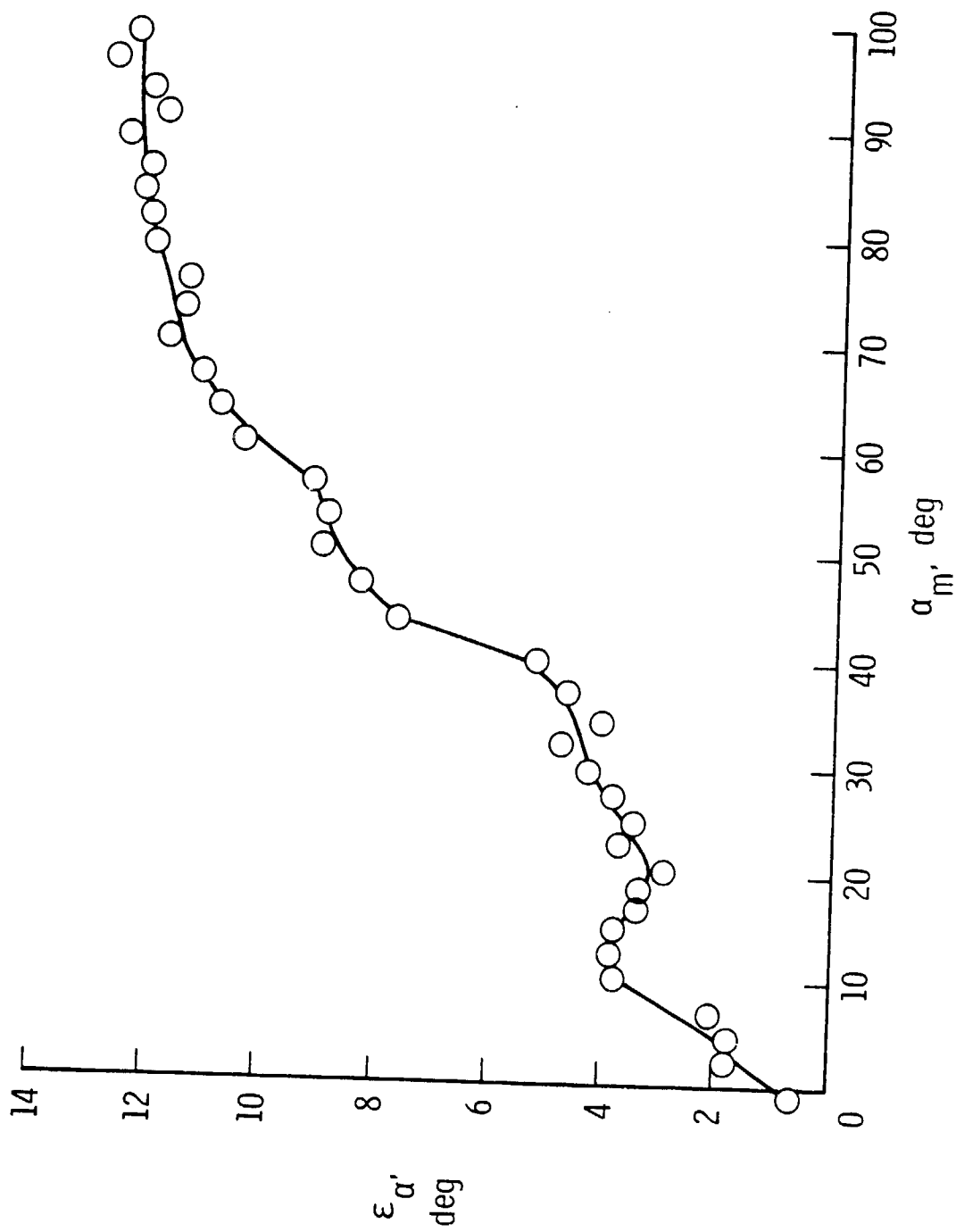


Figure 19.- The angle-of-attack flow correction determined from the static wind-tunnel tests.

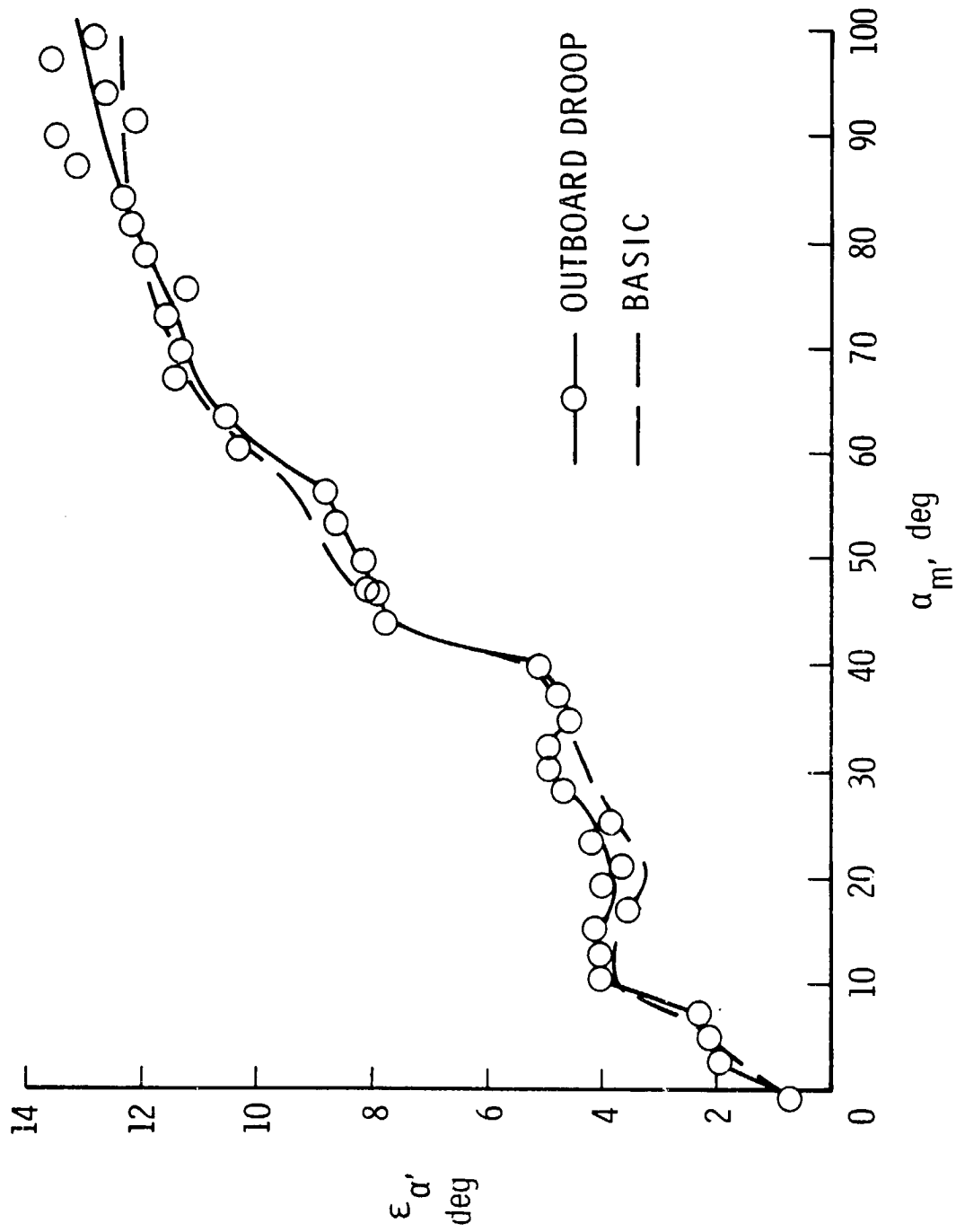


Figure 20.- The effect of the outboard droop leading-edge modification on the angle-of-attack flow correction determined from the static wind-tunnel tests.

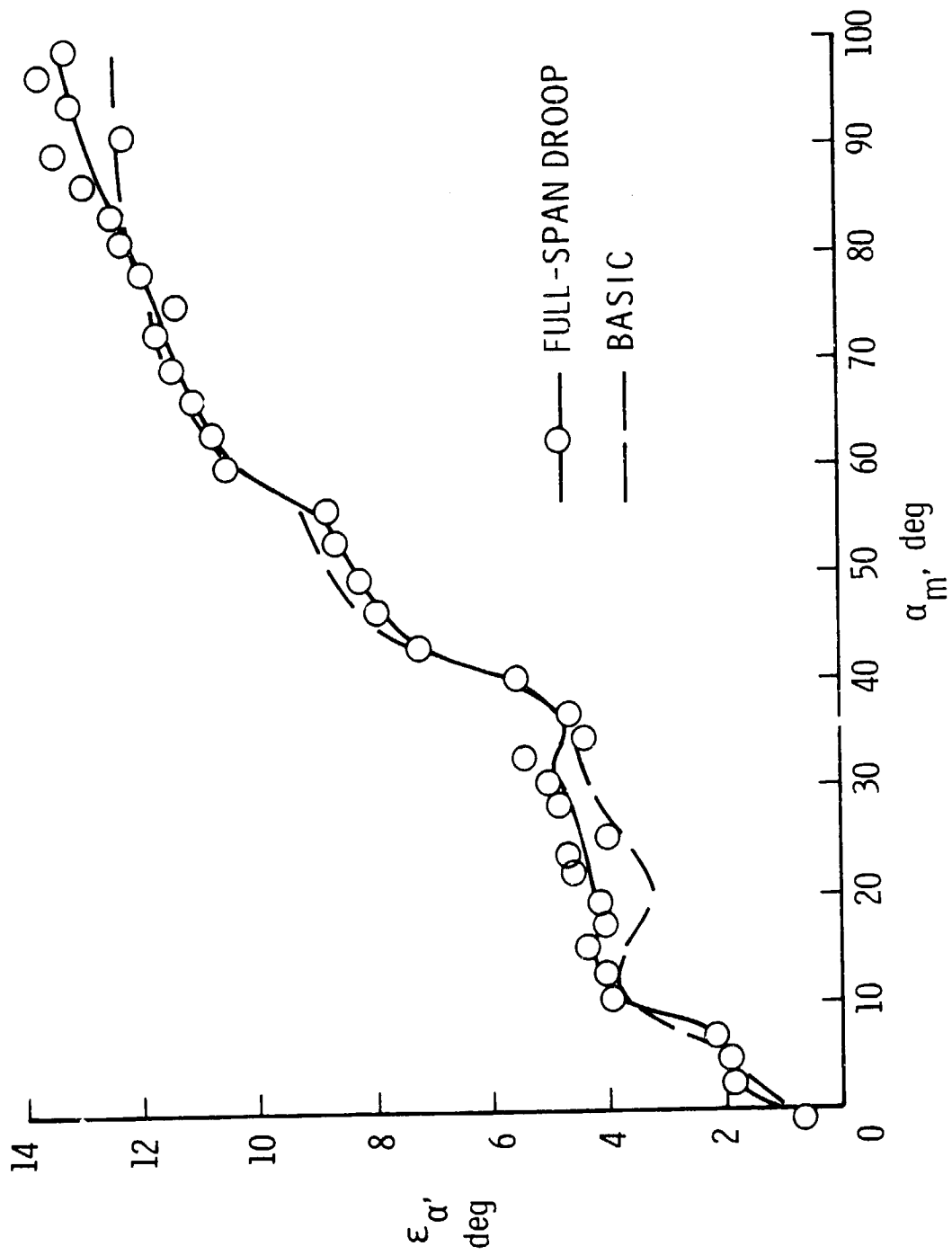


Figure 21.- The effect of the full-span droop leading-edge modification on the angle-of-attack flow correction determined from the static wind-tunnel tests.

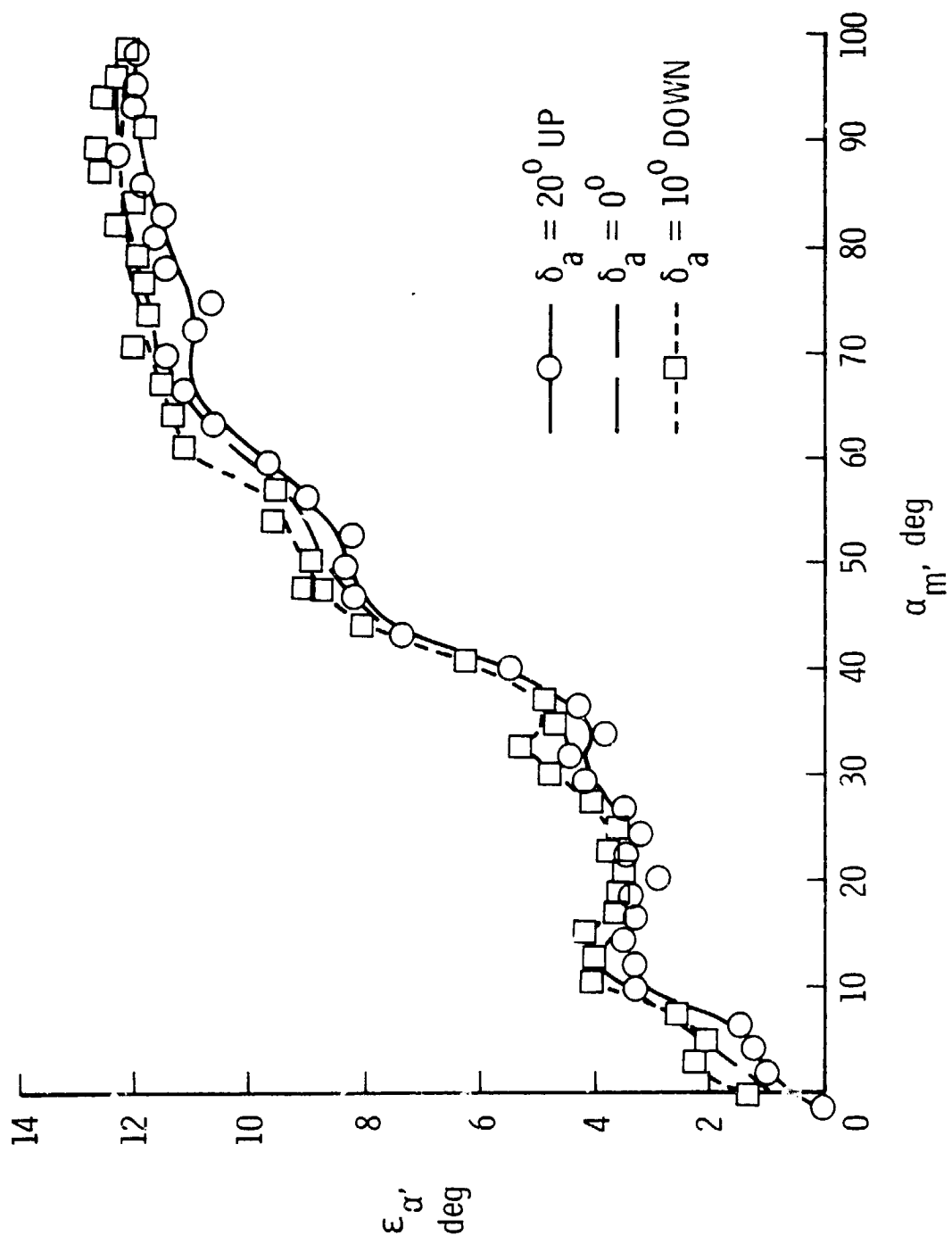


Figure 22.- The effect of aileron deflections on the angle-of-attack flow correction determined from the static wind-tunnel tests.

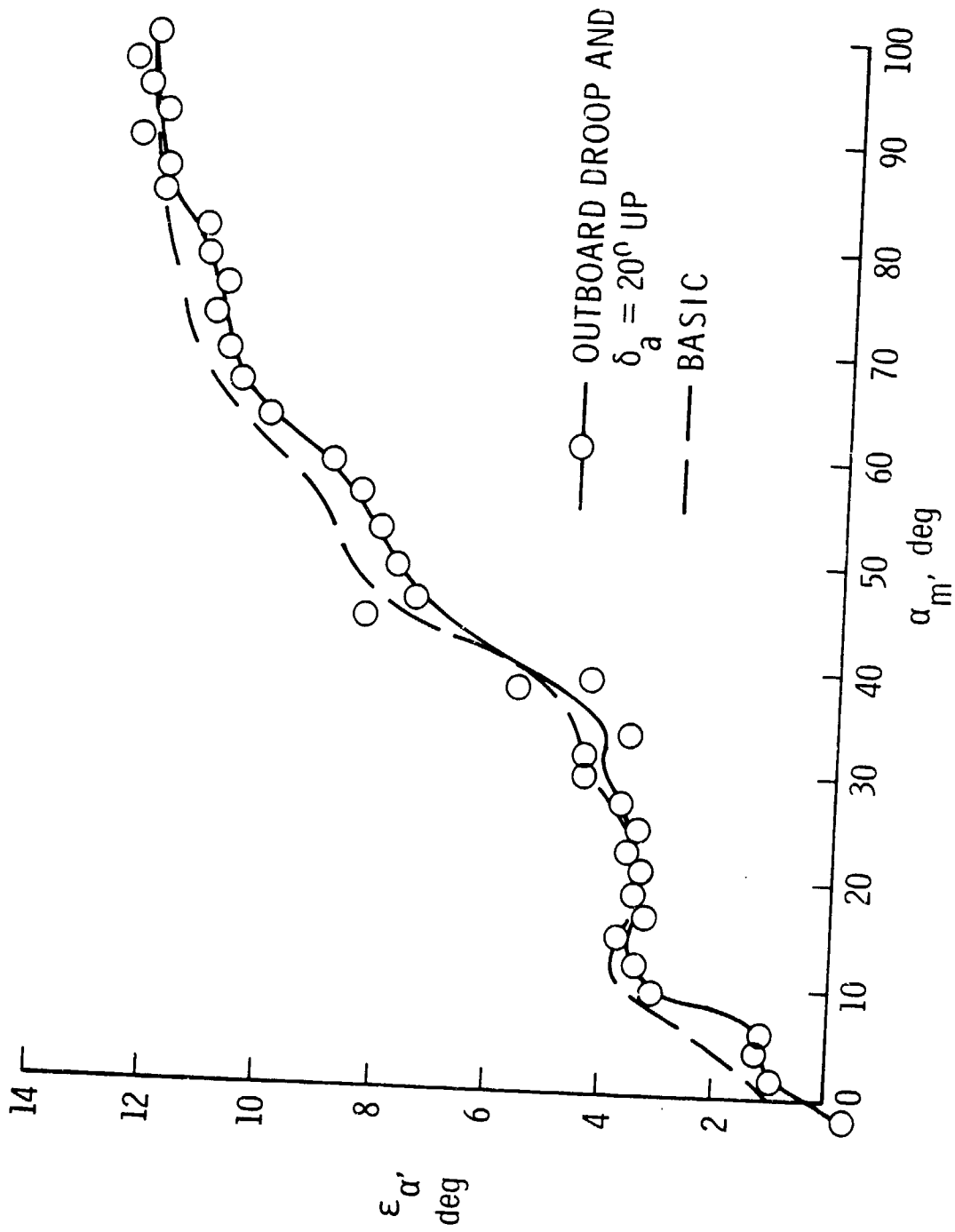


Figure 23.- The effect of the outboard droop modification and an aileron deflection on the angle-of-attack flow correction determined from the static wind-tunnel tests.

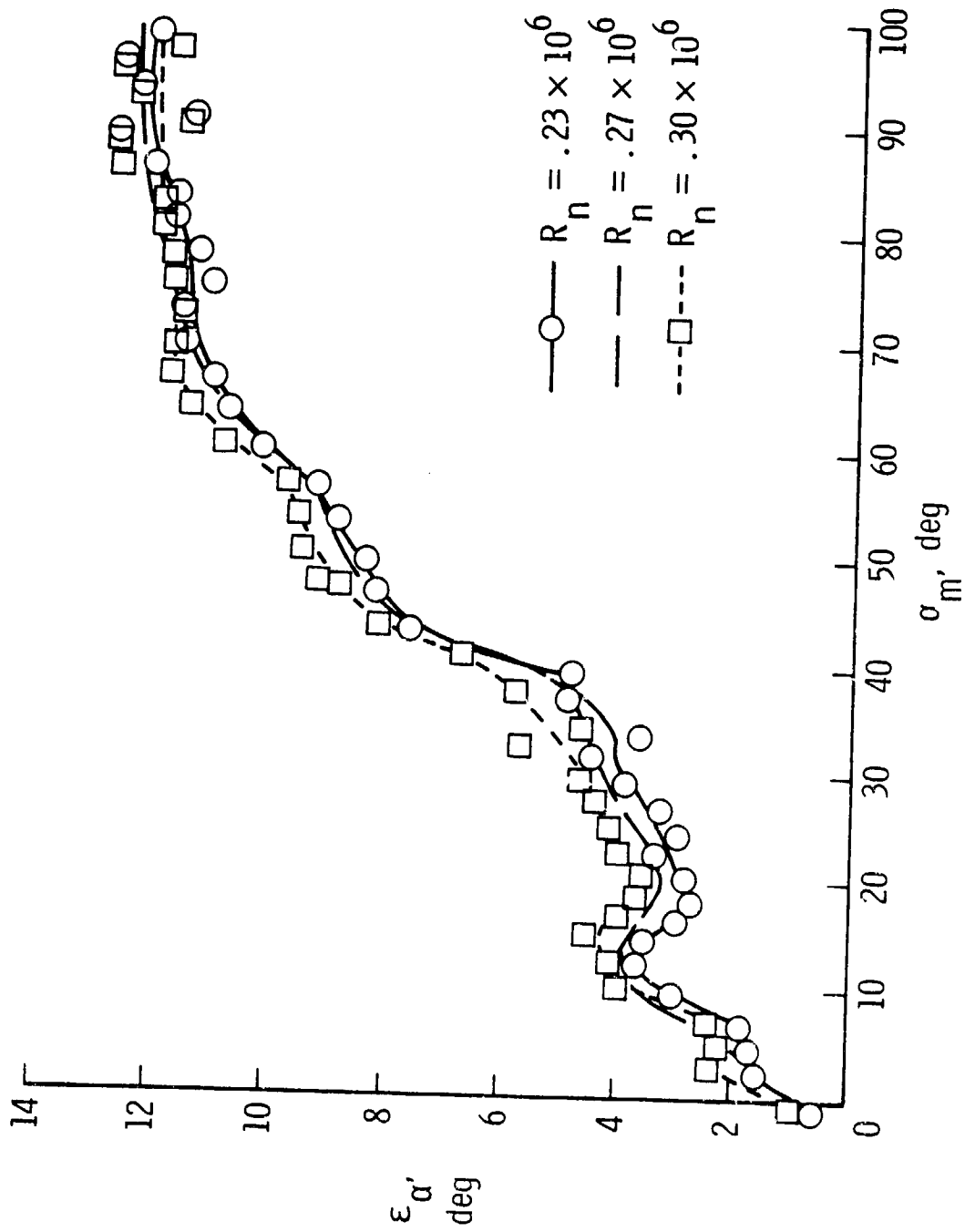


Figure 24.- The effect of the Reynolds number on the angle-of-attack flow correction determined from the static wind-tunnel tests.

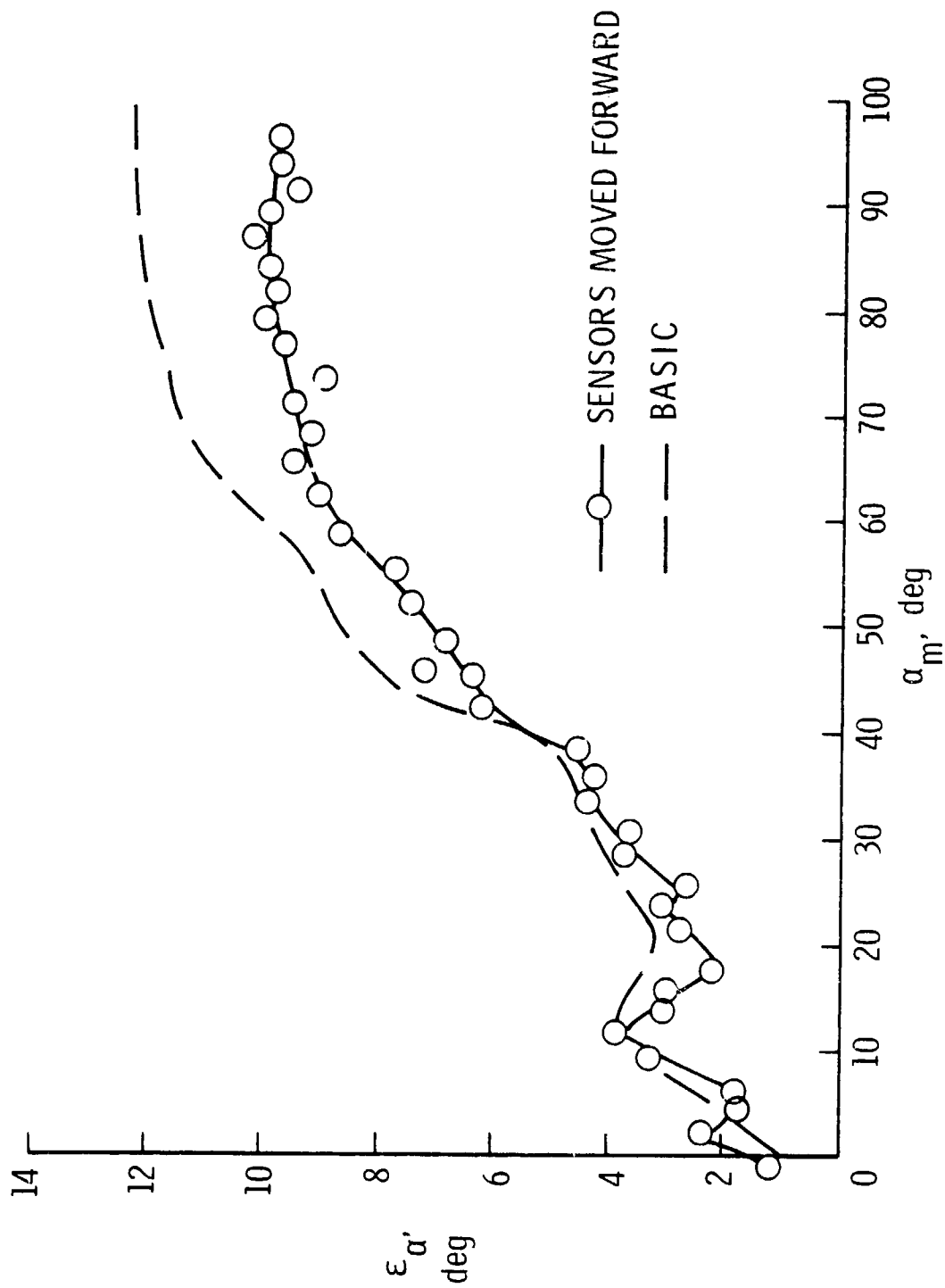


Figure 25.- The effect of the sensor location on the angle-of-attack flow correction determined from the static wind-tunnel tests.

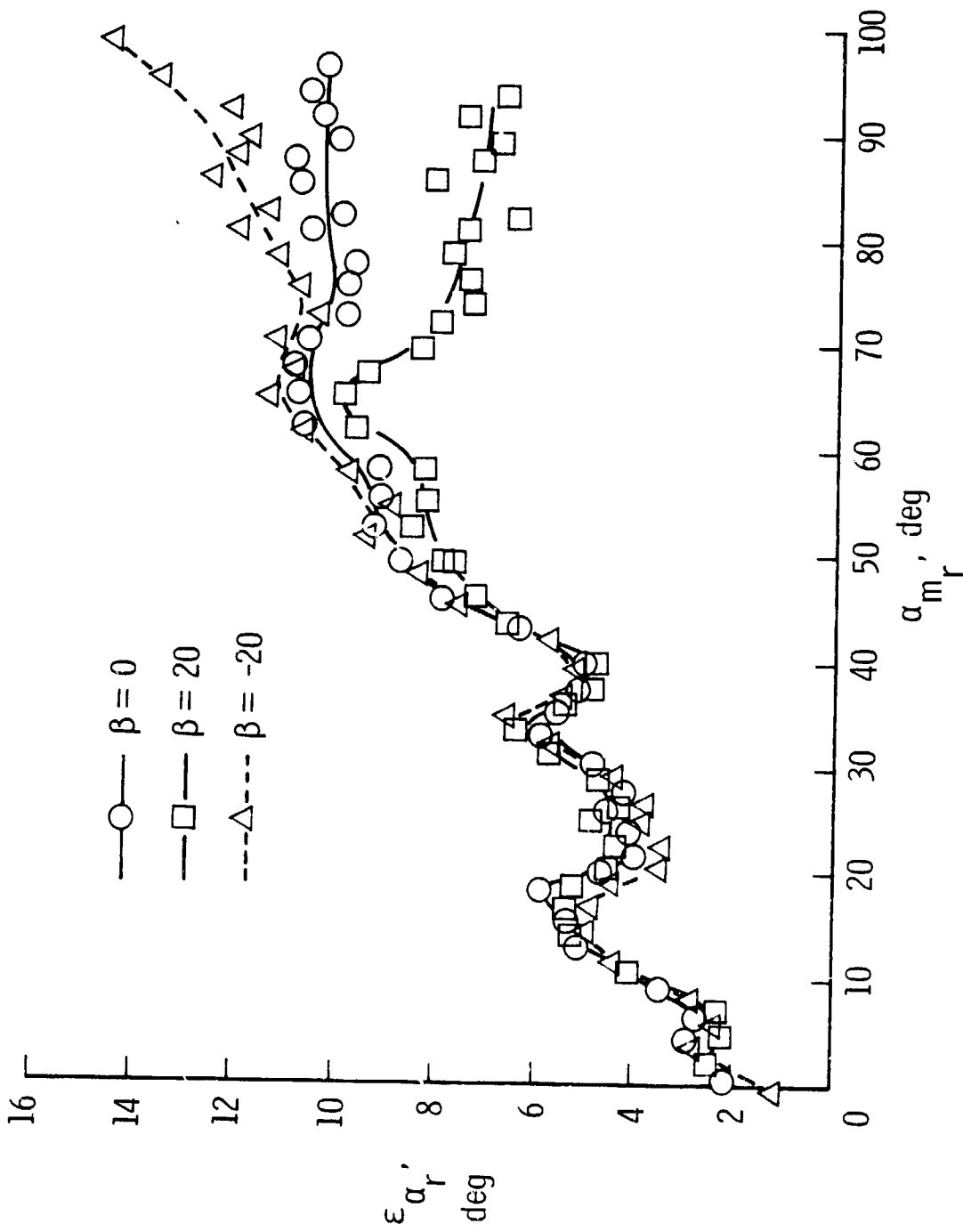


Figure 26.- The effect of the sideslip angle on the angle-of-attack flow correction determined from the static wind-tunnel tests.

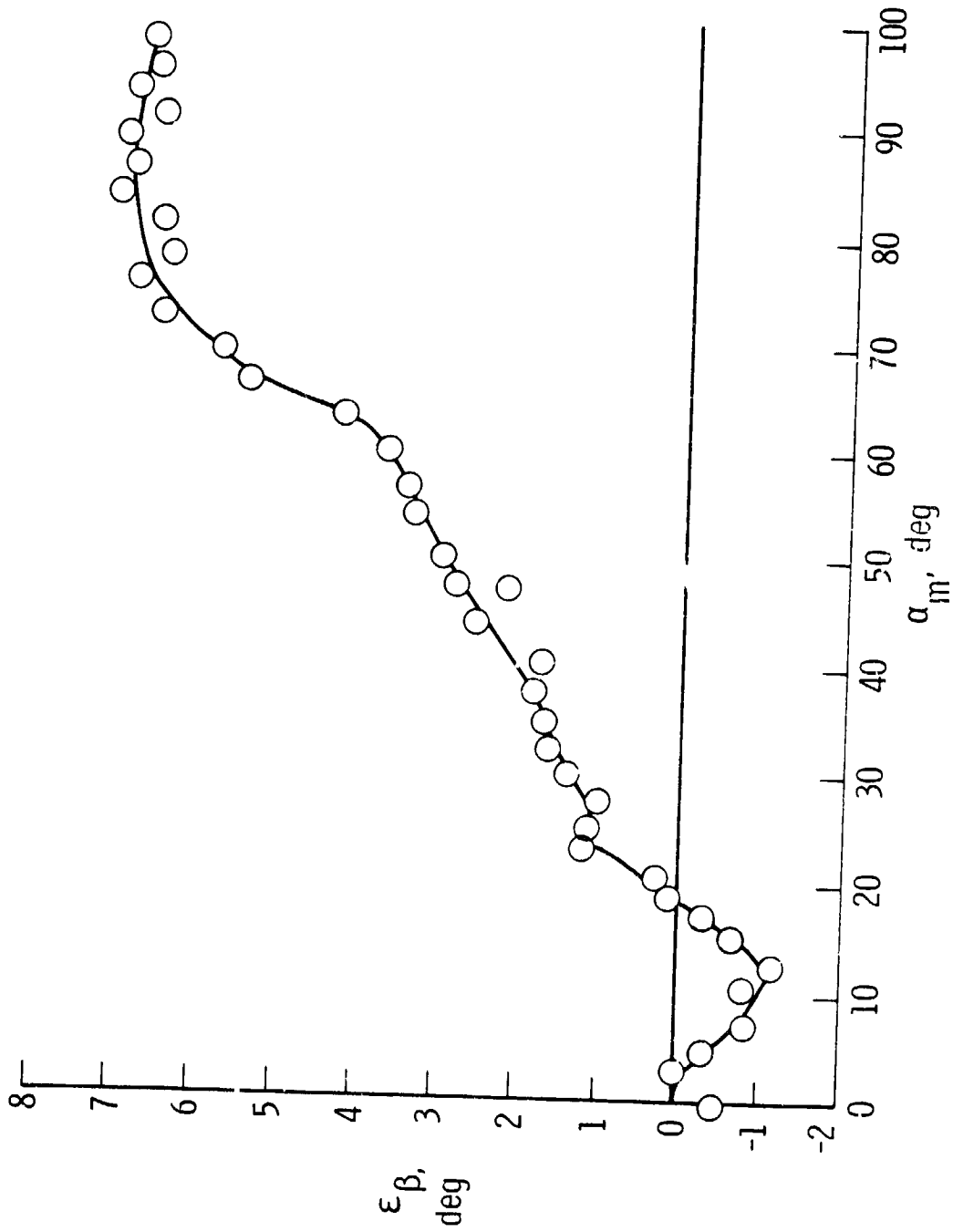


Figure 27.- The angle-of-sideslip flow correction determined from the static wind-tunnel tests.

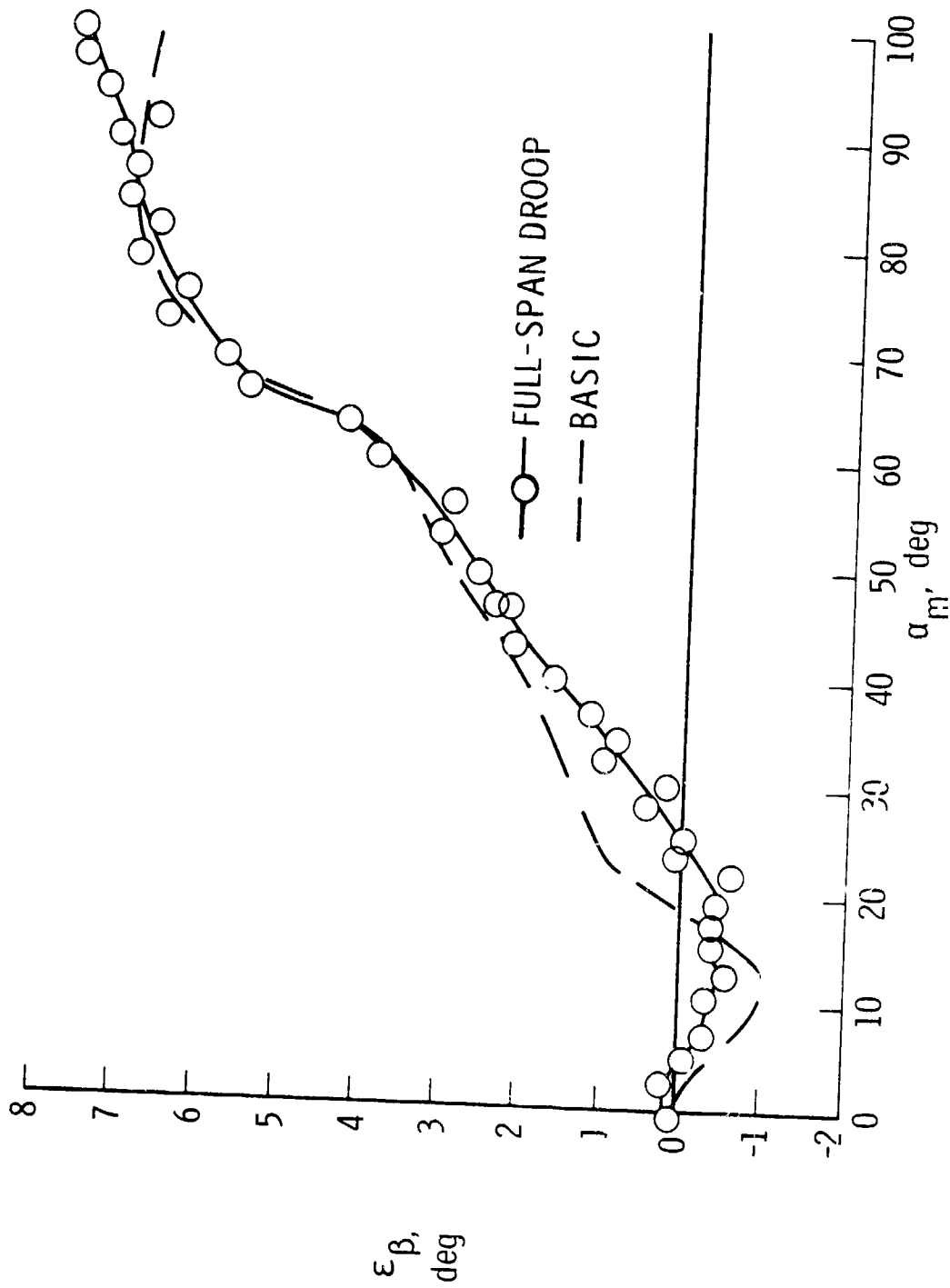


Figure 28.- The effect of the full-span droop leading-edge modification on the angle-of-sideslip flow correction determined from the static wind-tunnel tests.

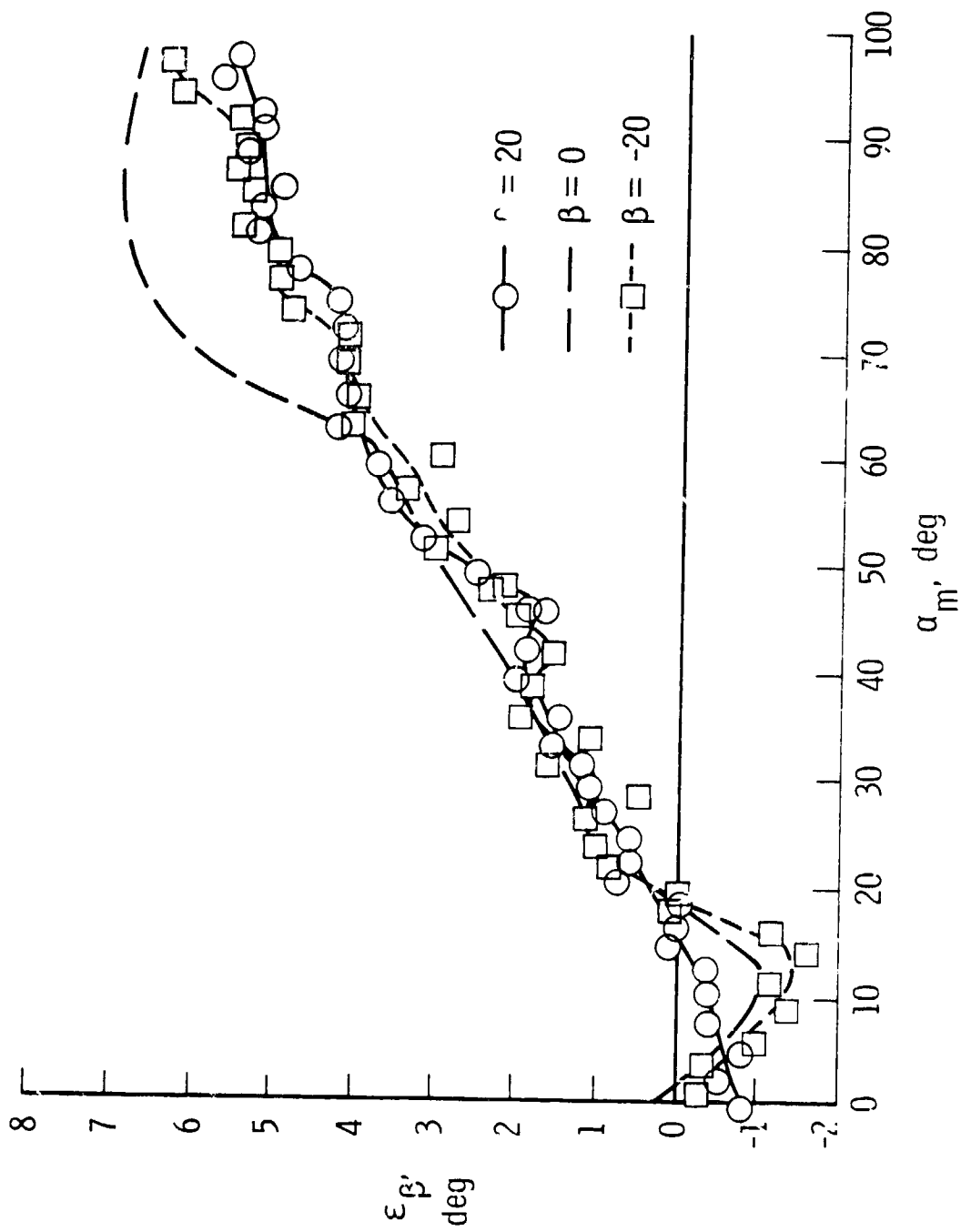


Figure 29.- The effect of the sideslip angle on the angle-of-sideslip flow correction determined from the static wind-tunnel tests.

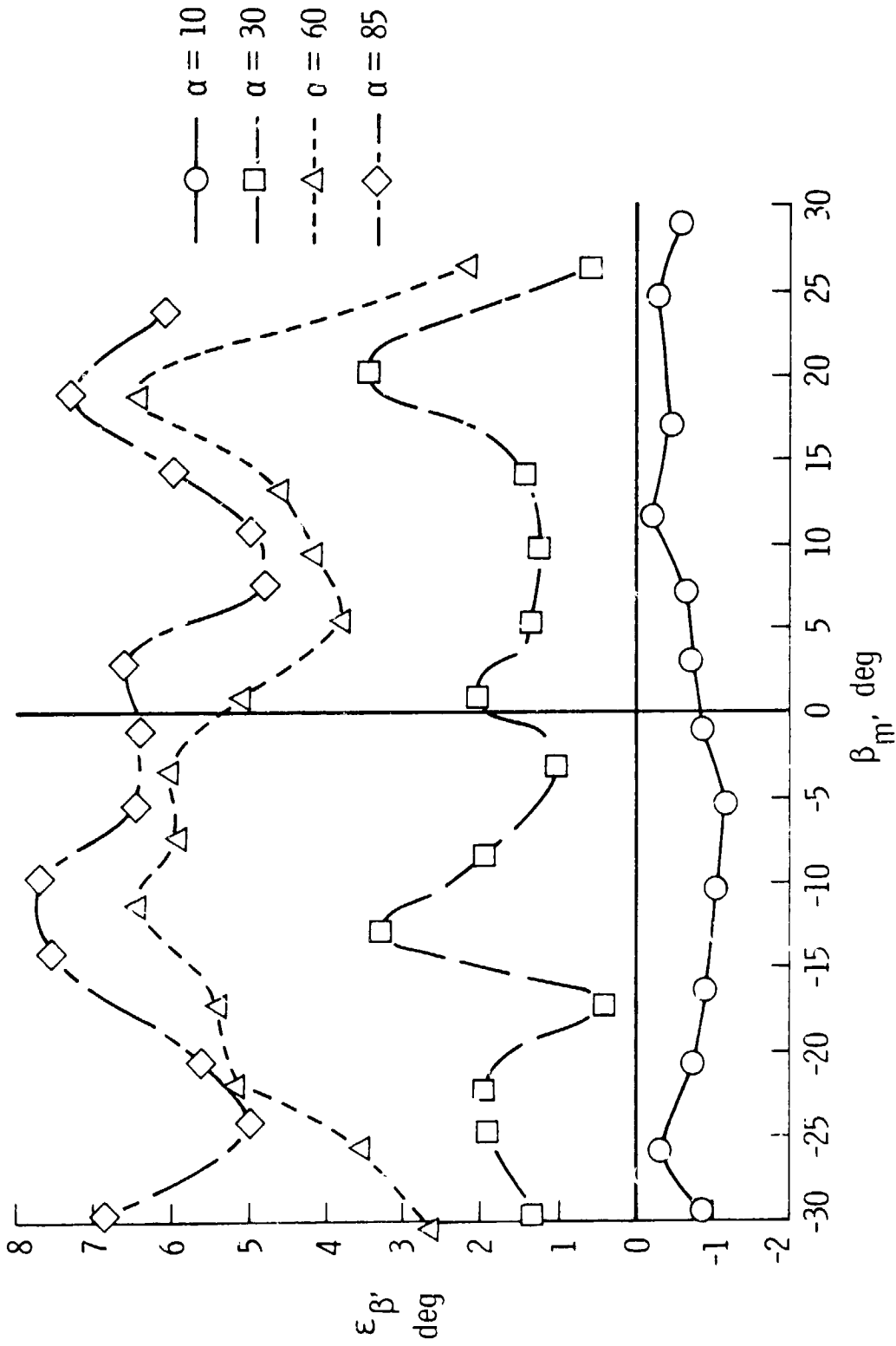


Figure 30.- The effect of the angle of attack on the angle-of-sideslip flow correction determined from the static wind-tunnel tests.

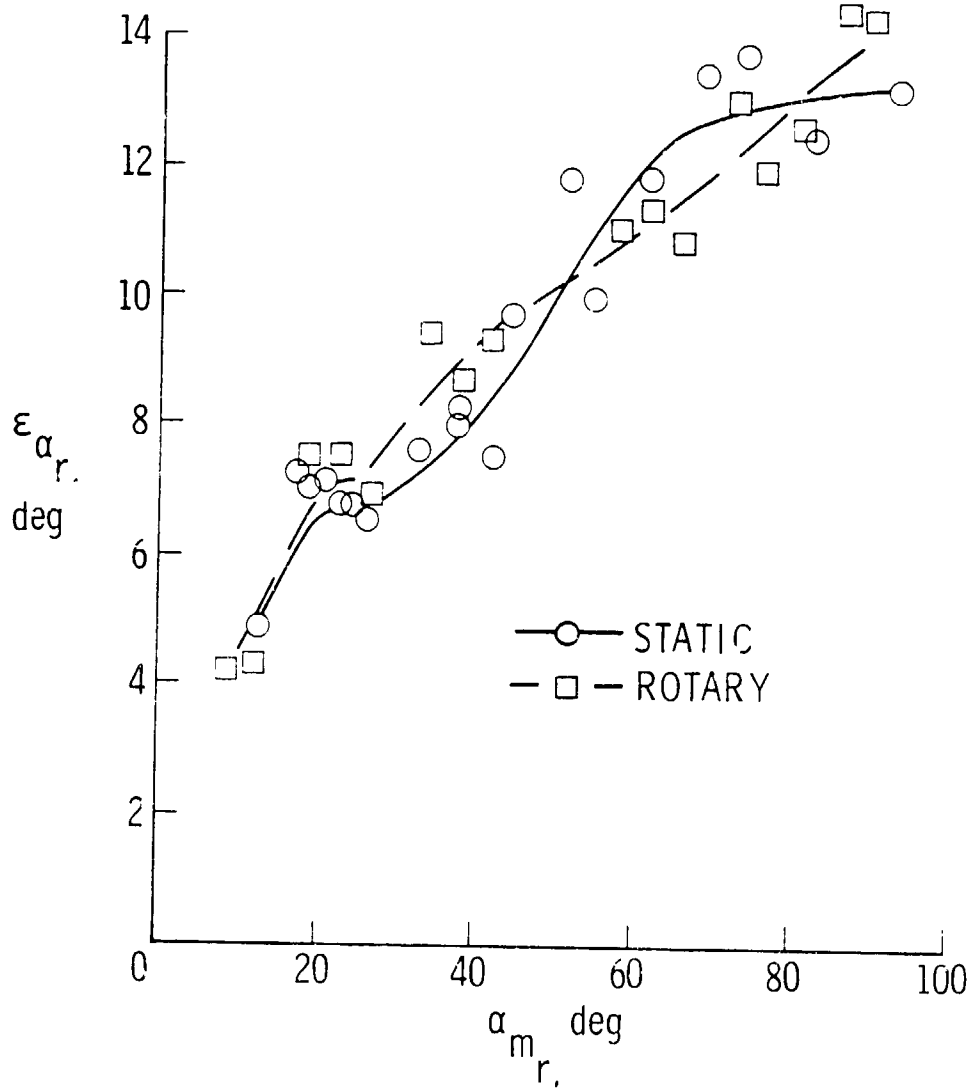


Figure 31.- The effect of rotation on the angle-of-attack flow correction determined in the spin tunnel. Determined from different rates of rotation at $\alpha_{t_{cg}} = 40^\circ$.

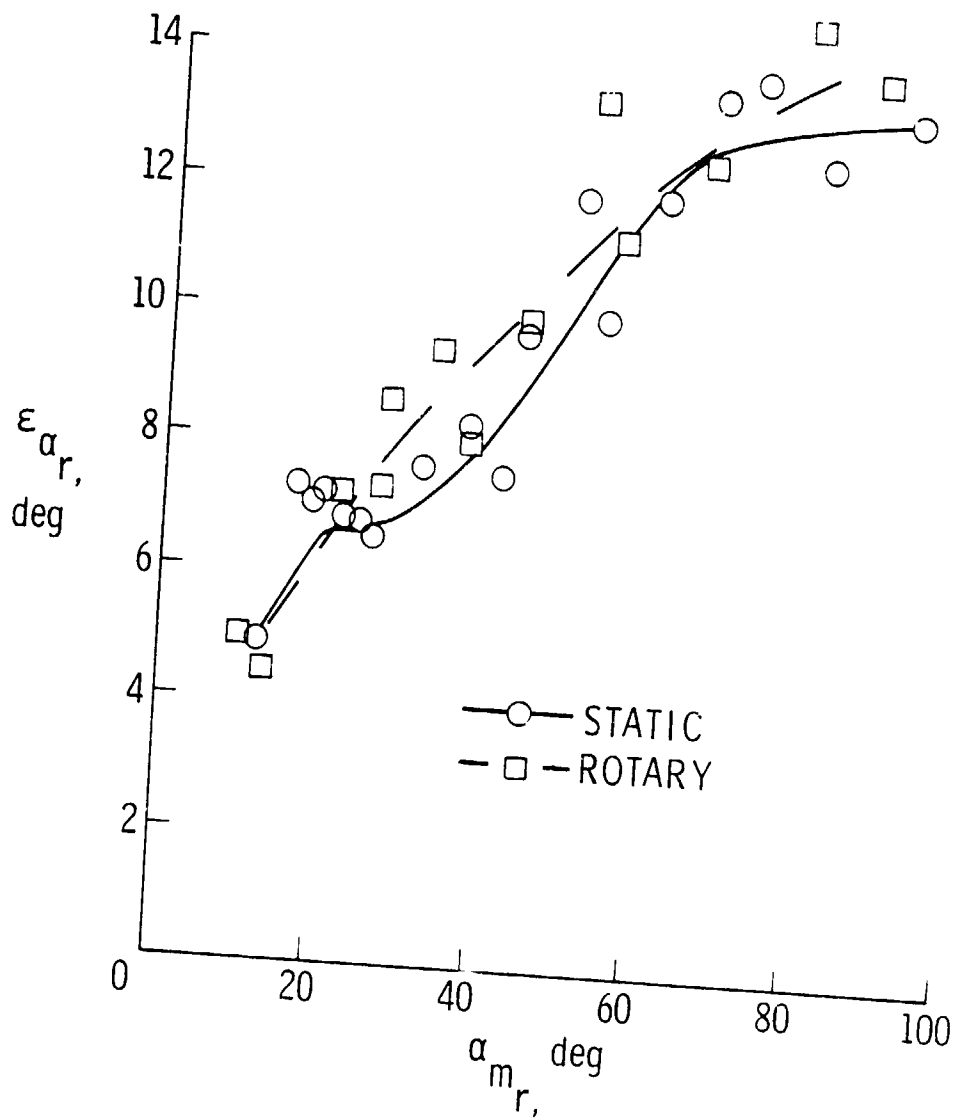


Figure 32.- The effect of rotation on the angle-of-attack flow correction determined in the spin tunnel. Determined from different angle-of-attack settings at $\beta b/2V = -.3$.

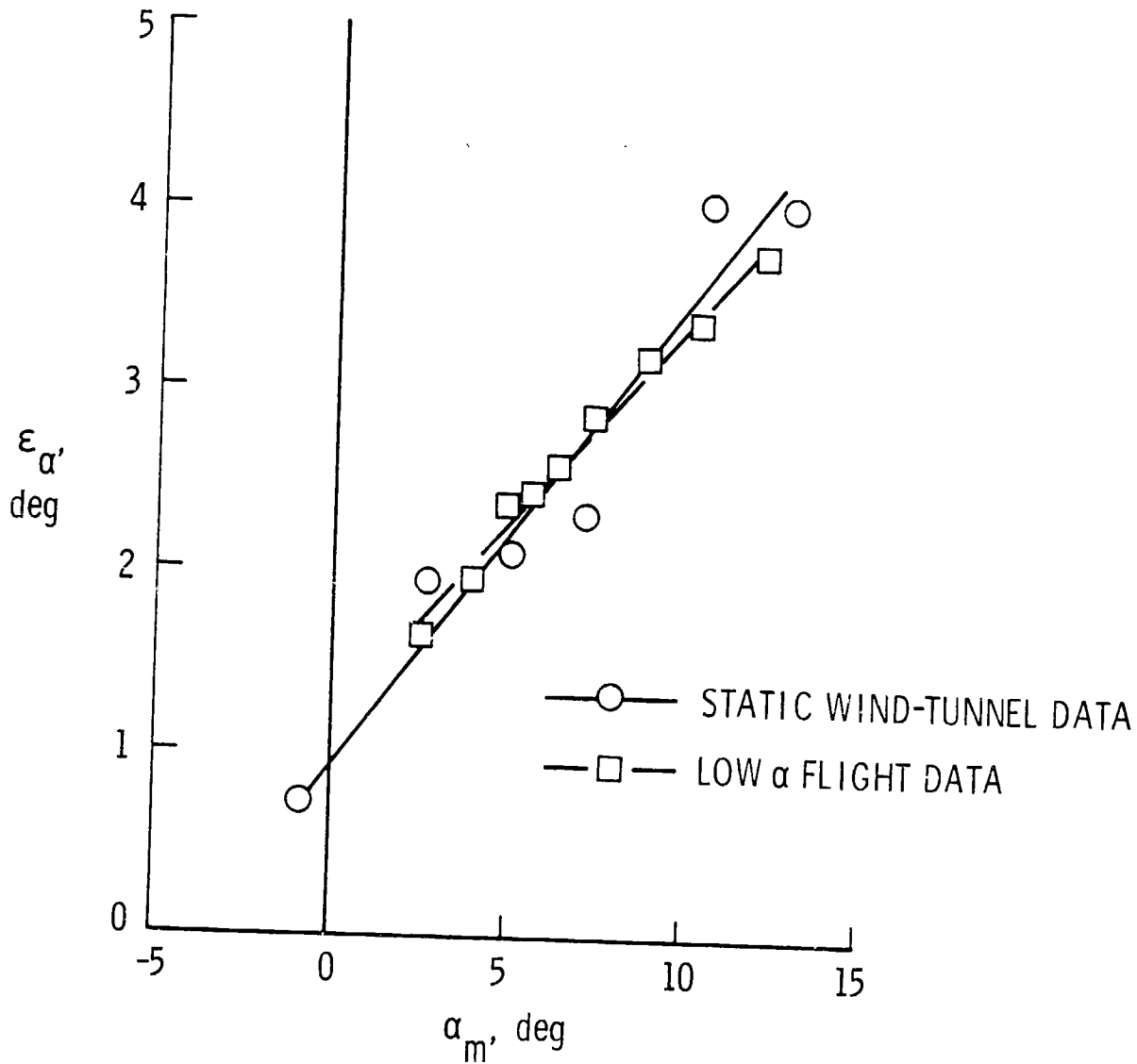


Figure 33.- Comparison of the angle-of-attack flow correction determined from static wind-tunnel tests and from level flight tests.

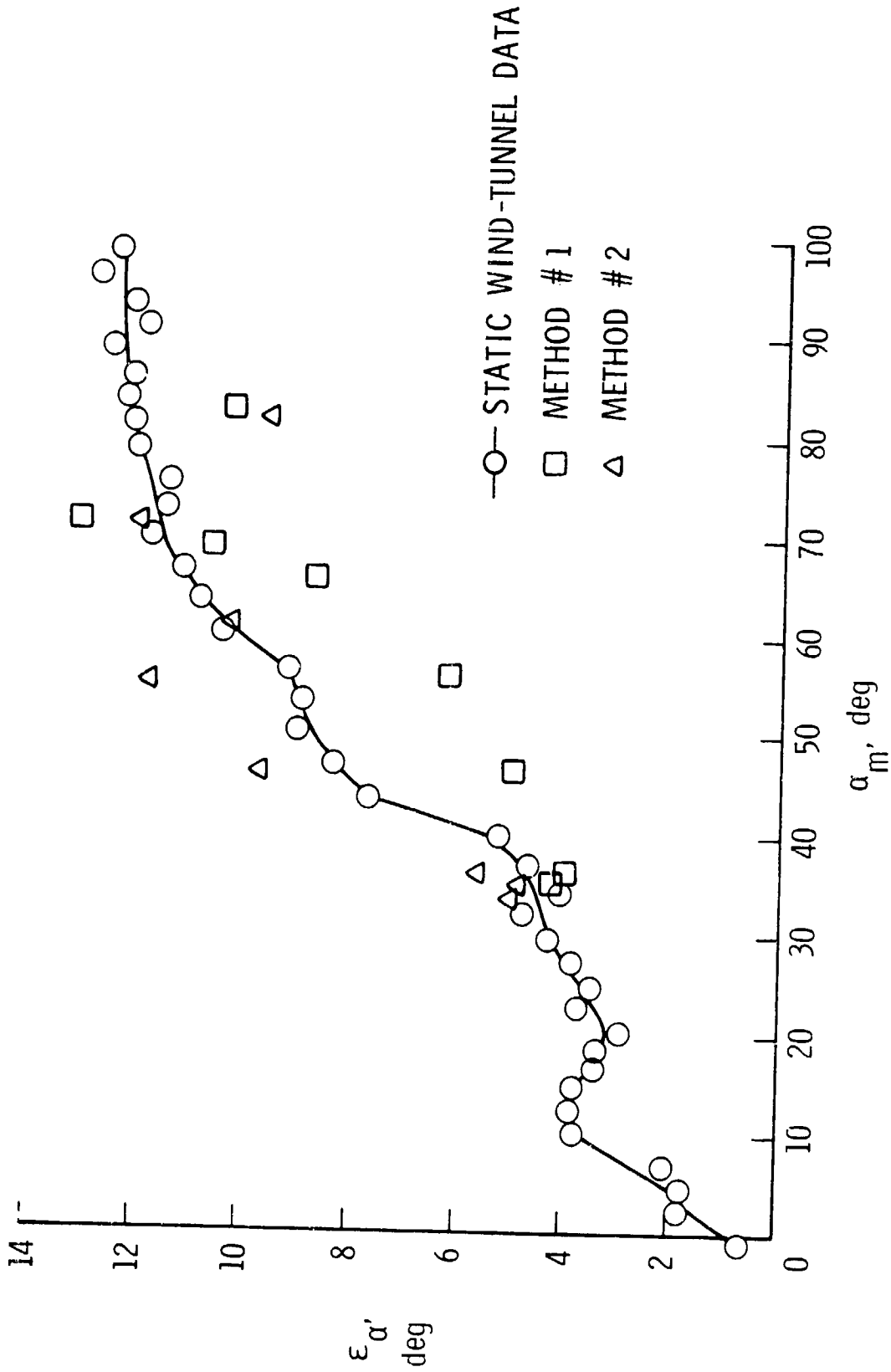


Figure 34.- Comparison of the angle-of-attack flow correction determined from static wind-tunnel tests and from two approximate methods used during steady spins.

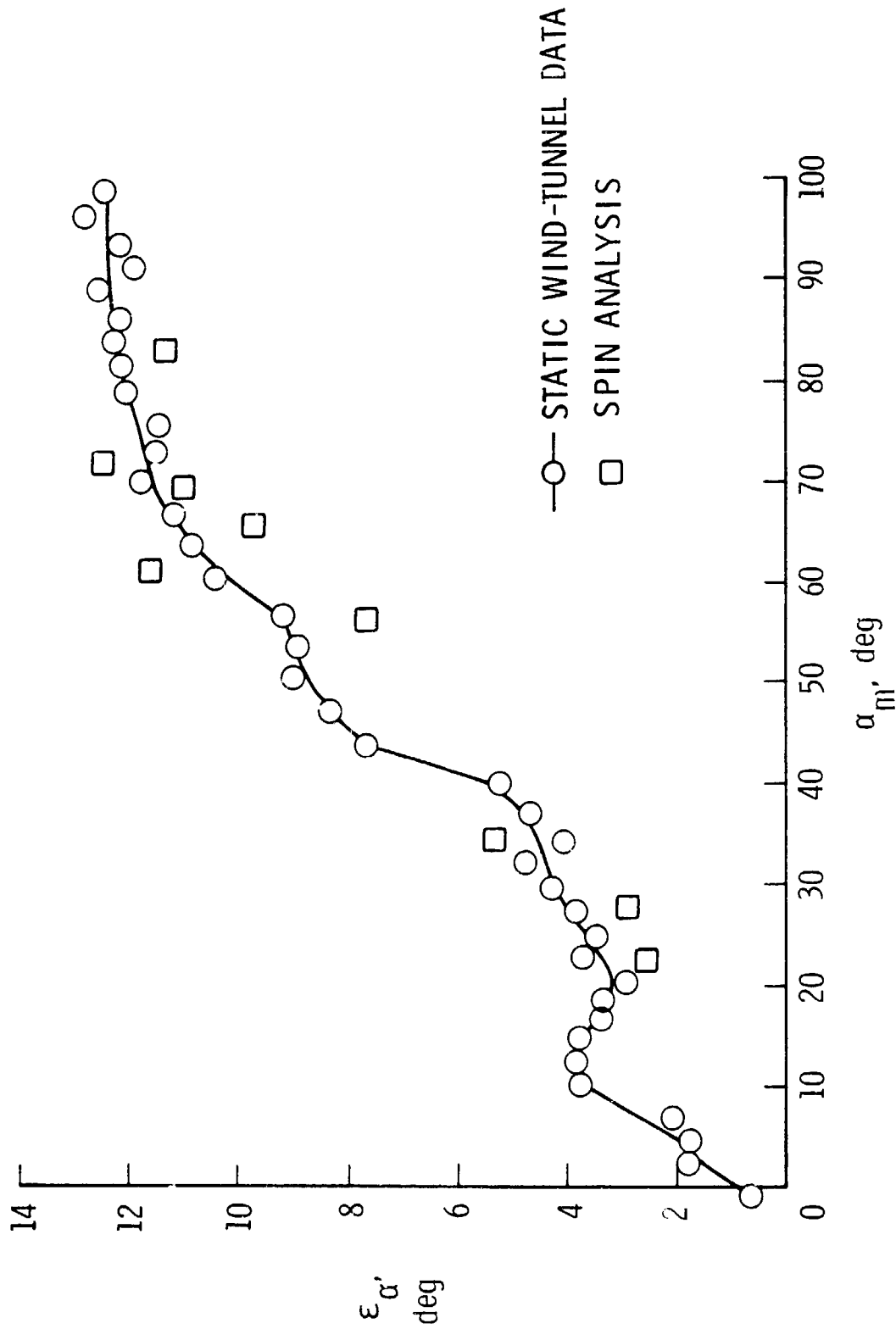


Figure 35.- Comparison of the angle-of-attack flow correction determined from static wind-tunnel tests and from a steady spin analysis technique.

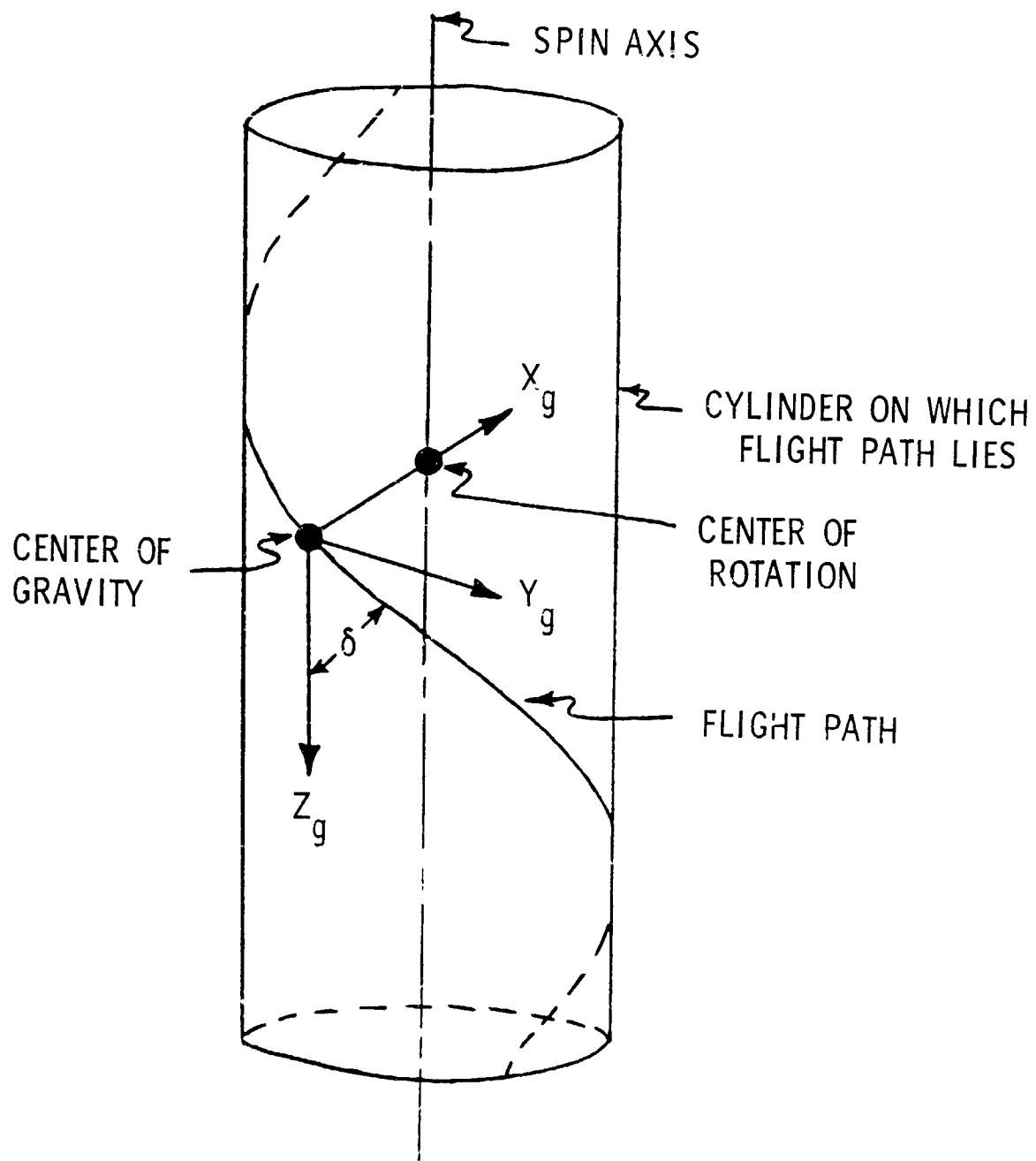


Figure 36.- Instantaneous arrangement of ground axis system.

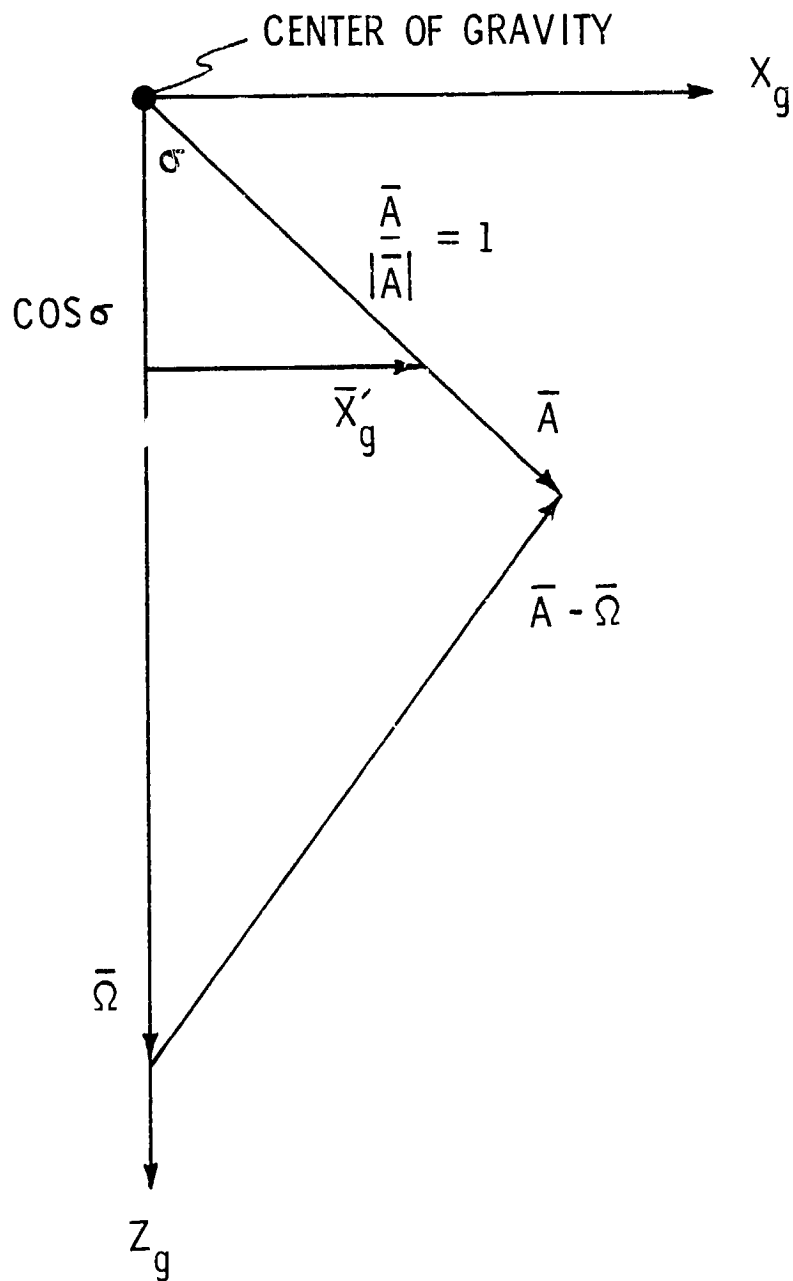


Figure 37.- Relationship between resultant acceleration and resultant rotation vectors.